

## CHAPTER IV

### RESULTS AND DISCUSSION

#### 4.1. Synthesis of oxidation of graphite

The graphite was oxidized with  $\text{H}_2\text{SO}_4/\text{NaNO}_3/\text{KMnO}_4$  under sonication. They could be partially separated from one another by centrifugation (Figure 4.2). Various shapes of carbon-based materials including tubes, sheets and spheres, were obtained (determined by SEM, TEM and HR-TEM). Centrifugation at 9,400 g resulted in precipitant of artifacts and large particles. The supernatant was then centrifuged at 11,300 g. The precipitant was re-dispersed in distilled water (Fraction 1, F1). The supernatant was centrifuged at 21,100 g. The precipitant was re-dispersed in distilled water (Fraction 2, F2). The supernatant was centrifuged at 37,600 g (Figure 4.1). The precipitant was re-dispersed in distilled water (fraction 3, F3) and the supernatant was used as fraction 4 (F4). After that the F4 was filtered by ultrafiltration (pore size of 100 nm) to obtain fraction 5 (F5). Each fraction was characterized by UV-Vis spectrometry, SEM, TEM, HR-TEM, SAED, ATR-FTIR, Raman spectroscopy, EA, TGA, XPS, DLS, and CLSFM.



Figure 4. 1 Picture of F3 suspension at 100 ppm in water (left) and F4 suspension at 100 ppm in water (right).

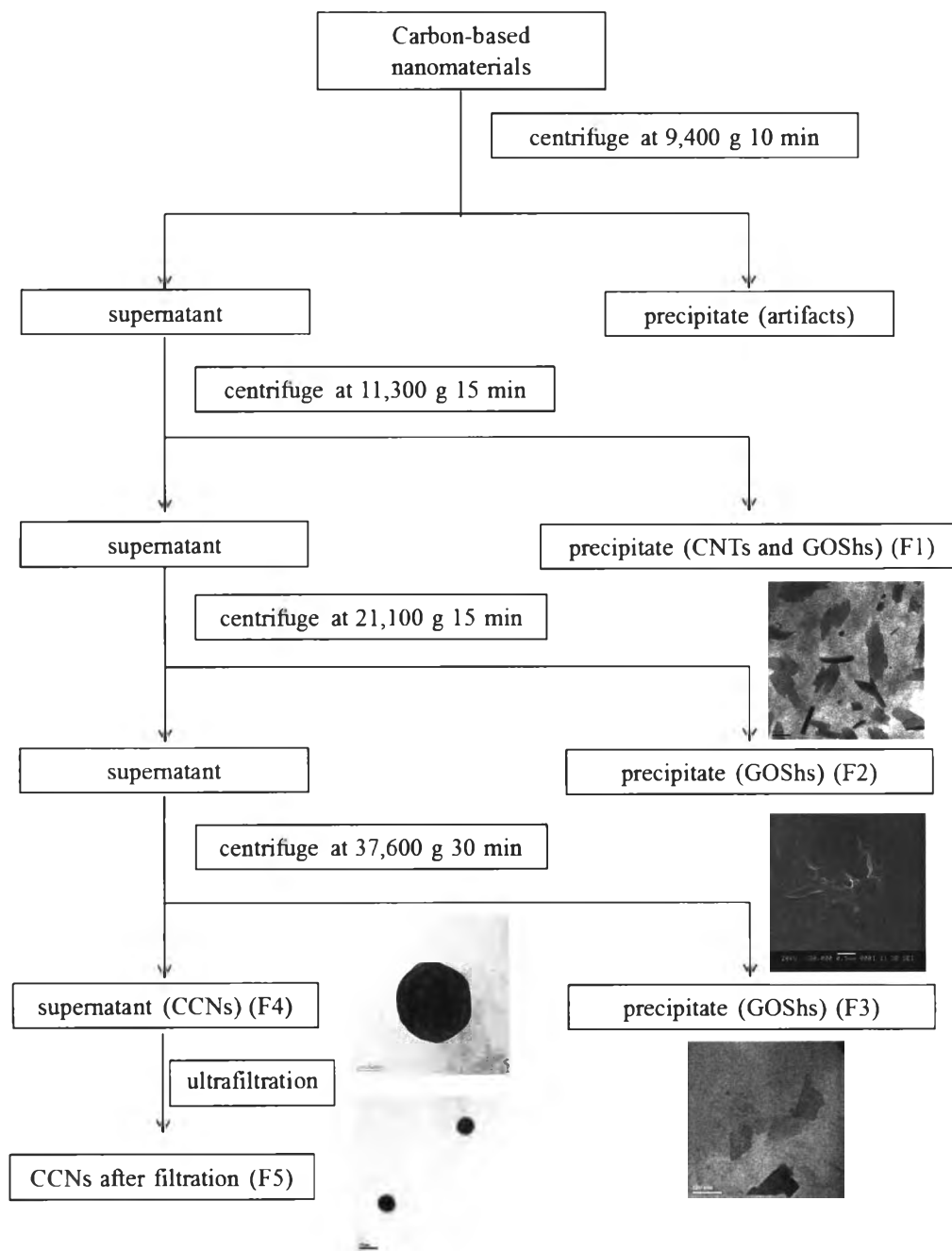


Figure 4. 2 Separation of carbon-base nanomaterials



## 4.2. Characterization

The structural characterization was carried out by UV-Vis spectroscopy, SAED, ATR-FT-IR, Raman spectroscopy, XPS, and EA. The morphology was characterized by SEM, TEM and HR-TEM. The particles size was analyzed by DLS.

**Table 4. 1 The structural and morphology characterization of carbon-base materials**

Samples	Structural characterization	Morphology characterization
Fraction 1 (F1)	-	TEM
Fraction 2 (F2)	-	SEM
Fraction 3 (F3)	UV-Vis absorption, SAED, ATR-FT-IR, Raman spectroscopy, XPS, and EA	TEM and HR-TEM
Fraction 4 (F4)	UV-Vis absorption, SAED, ATR-FT-IR, Raman spectroscopy, XPS, and EA	SEM, TEM and HR-TEM
Fraction 5 (F5)	-	TEM



## The morphology characterization

### 4.2.1 Scanning electron microscopy (SEM)

SEM photographs of F2 and F4 are shown in Table 4.2. The SEM photograph showed sheet like materials for F2 and spherical architecture for F4. The average diameter of F4 calculated from SEM image (30,000x) was  $129.6 \pm 0.1$  nm.

**Table 4. 2 SEM photographs of F2 and F4**

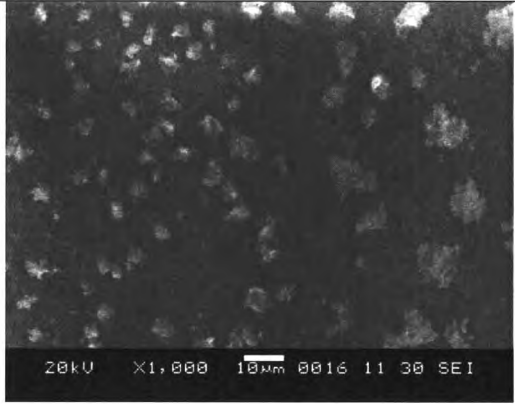

Samples	Magnification	Scale bar ( $\mu\text{m}$ )	SEM photograph
F2	1000x	10	
	30,000x	0.5	



Table 4. 2 SEM photographs of F2 and F4 (continued)

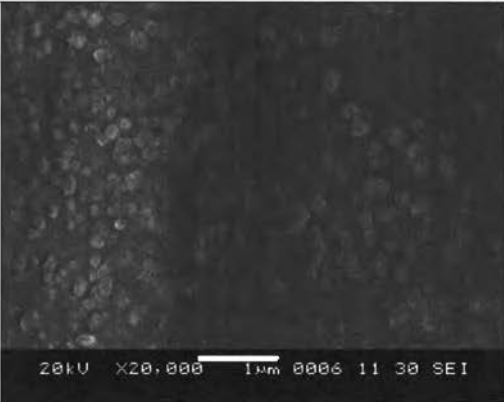
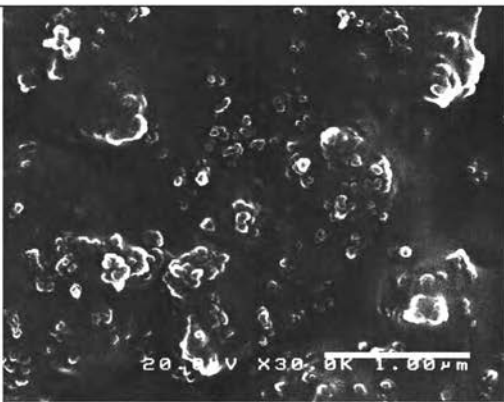
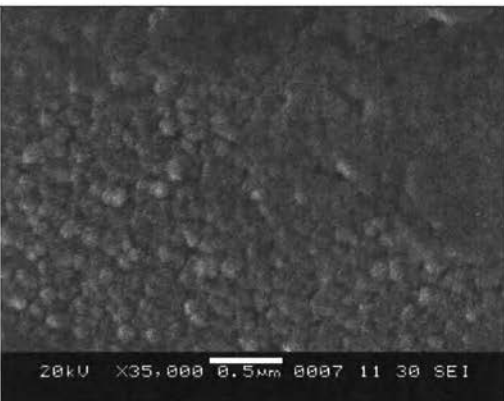

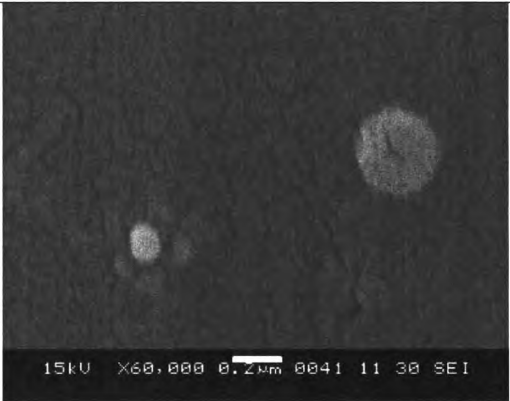
Samples	Magnification	Scale bar ( $\mu\text{m}$ )	SEM photograph
F4	20,000x	1	
	30,000x	1	
	35,000x	0.5	



Table 4. 2 SEM photographs of F2 and F4 (continued)

Samples	Magnification	Scale bar ( $\mu\text{m}$ )	SEM photograph
F4	60,000x	0.5	
		0.2	



#### 4.2.2 Transmission electron microscopy (TEM)

TEM photographs of F1, F3, F4 and F5 are shown in Table 4.3. The TEM images of F1 showed sheets like particulates mixed with rod-shape particles. The length range was 500-1,000 nm. The TEM images of F3 showed sheets like material with size range of 100-300 nm. The TEM images of F4 showed spherical shape with size range of 100-200 nm. The TEM images of F5 showed spherical shape with size less than 100 nm.

Table 4. 3 TEM photographs of F1, F3, F4 and F5

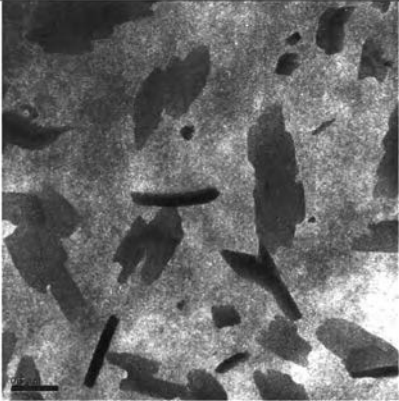
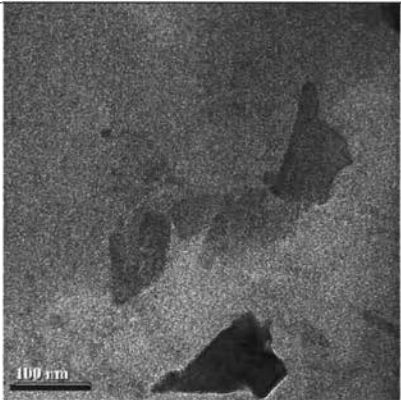
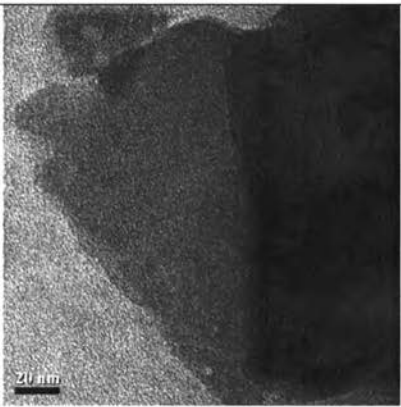
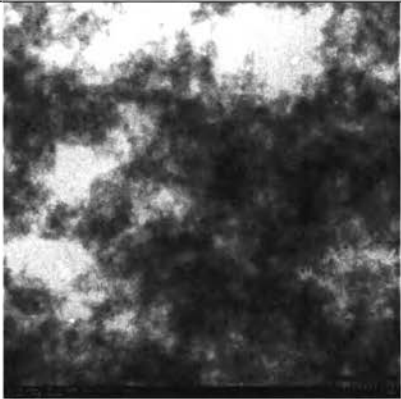
Samples	Magnification	Scale bar ( $\mu\text{m}$ )	TEM images
F1	5,000x	0.5	



Table 4. 3 TEM photographs of F1, F3, F4 and F5 (continued)

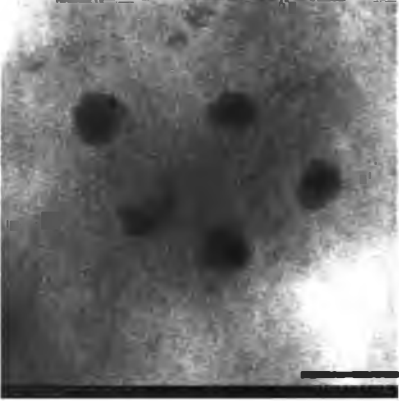
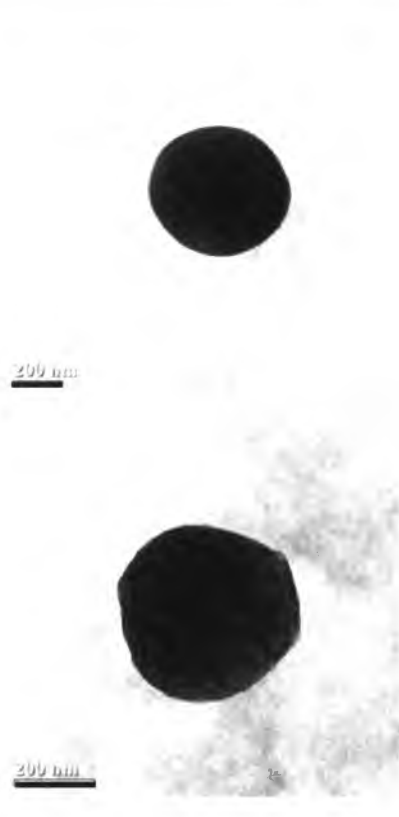
Samples	Magnification	Scale bar ( $\mu\text{m}$ )	TEM images
F3	20,000x	0.1	
	40,000x	0.02	
F4	1,200x	1	



137614976



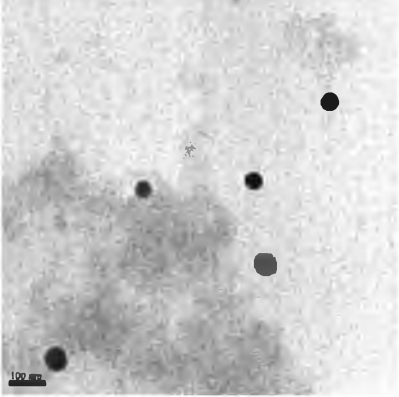
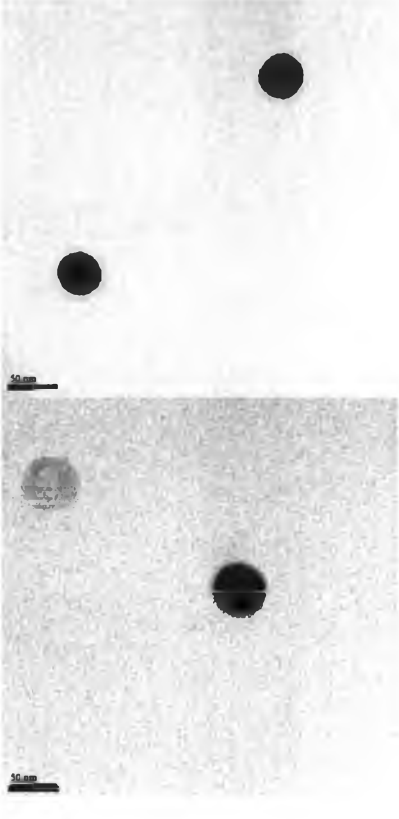
Table 4. 3 TEM photographs of F1, F3, F4 and F5 (continued)

Samples	Magnification	Scale bar ( $\mu\text{m}$ )	TEM images
F4	20,000x	0.2	
	60,000x	0.2	



137614976

Table 4. 3 TEM photographs of F1, F3, F4 and F5 (continued)

Samples	Magnification	Scale bar ( $\mu\text{m}$ )	TEM images
F5	20,000x	0.1	
	50,000x	0.05	



### 4.2.3 High-resolution transmission electron microscopy (HR-TEM)

To investigate morphology in detail, high-resolution transmission electron microscopy was used. The HR-TEM photographs of F3 and F4 are shown in Table 4.4. The HR-TEM photograph of F3 showed sheet-like material with 6-8 layers (400,000x with 6x digital zoom). The HR-TEM photographs of F4 showed spherical shape (1,000x and 20,000x). The 100,000x HR-TEM photographs of F4 showed aggregation of many hollow spherical shapes with a diameter of  $\sim 5$  nm. The result indicated that circular structures in F4 are large spherical aggregated of numeral small spherical particles (F4, 100,000x).

Table 4. 4 HR-TEM photographs of F3 and F4

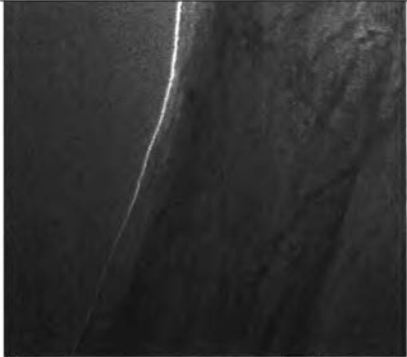
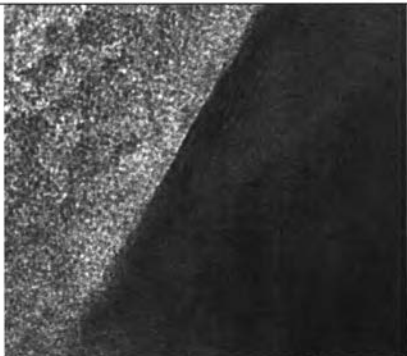
Samples	Magnification	Scale bar ( $\mu\text{m}$ )	HR-TEM photographs
F3	1,000x	2	
	400,000x	0.005	



Table 4. 4 HR-TEM photographs of F3 and F4 (continued)

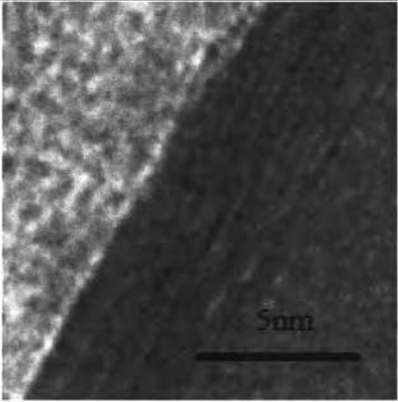
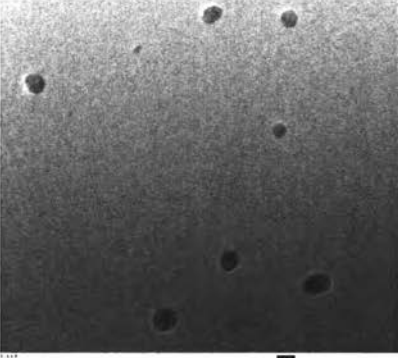
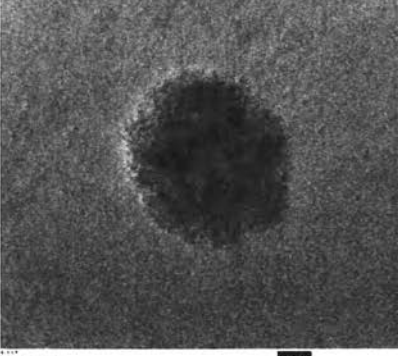
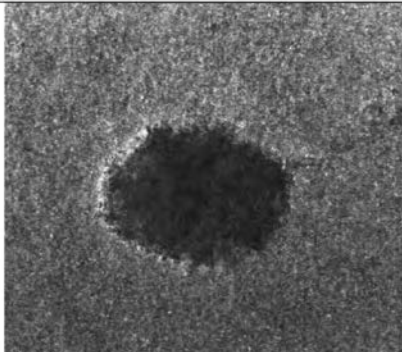
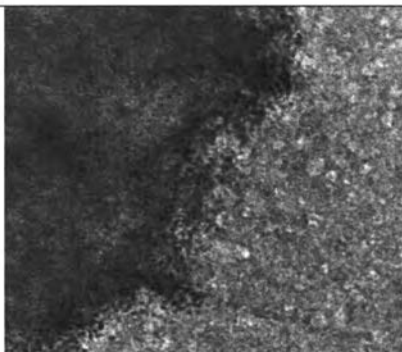
Samples	Magnification	Scale bar ( $\mu\text{m}$ )	HR-TEM photographs
F3	400,000x with X6 digital zoom	0.005	
F4	1,000x	0.5	
	20,000x	0.1	



Table 4. 4 HR-TEM photographs of F3 and F4 (continued)

Samples	Magnification	Scale bar ( $\mu\text{m}$ )	HR-TEM photographs
F4	20,000x	0.1	 <p>0.1 <math>\mu\text{m}</math></p>
	100,000x	0.02	 <p>0.02 <math>\mu\text{m}</math></p>



#### 4.2.4 Dynamic light scattering (DLS)

To analyze hydrated particle size, dynamic light scattering (DLS) was used. The average hydrated diameter and zeta potential of F3 and F4 are shown in Table 4.5. The size distribution profiles of both samples are shown in appendix A. The average hydrated diameter and surface charge of F3 were  $271.1 \pm 7.22$  nm and  $-50.21 \pm 0.73$  mV, respectively. The average hydrated diameter and surface charge of F4 were  $132.1 \pm 4.74$  nm and  $-47.56 \pm 1.18$  mV, respectively. The average diameter of F4 obtained from DLS is quite similar to that of  $110.8 \pm 0.09$  nm obtained from SEM. The highly negatively charged surface (more than  $-30$  mV) of both particles indicated good stability in water<sup>183</sup>.

**Table 4. 5 Physicochemical characteristics of carbon-based materials**

Sample	Particle size distribution from SEM	Particle size distribution from DLS	PDI	$\zeta$ potential
F3	-	$271.1 \pm 7.22$	0.414	$-50.21 \pm 0.73$
F4	$110.8 \pm 0.09$	$132.1 \pm 4.74$	0.387	$-47.56 \pm 1.18$

From SEM, TEM and HR-TEM images of water dispersible particles, various obtained from the process, it can be concluded that F1 was a mixture of large (500-5000 nm) rod and sheet particles whereas F2 and F3 were mostly carbon sheet with decreasing in size (200-5000 nm and 100-300 nm, respectively), and F4 and F5 were aggregate of many small spherical particles. Size of F4 was 100-200 nm while F5 was smaller than 100 nm. DLS indicated that F3 and F4 were stably dispersed in aqueous solution. F3 and F4 were selected for further characterization due to their good dispersible, desirable sized and morphology.



## The structural characterization

### 4.2.5 UV-spectroscopy

The UV-Vis absorption spectra of F3 and F4 were similar with a maximum absorption at 227 nm and an extended absorption up to 600 nm (Figure 4.3), which corresponded well with the presence of an extended  $\pi$ - $\pi$  conjugation network<sup>53 58</sup>.

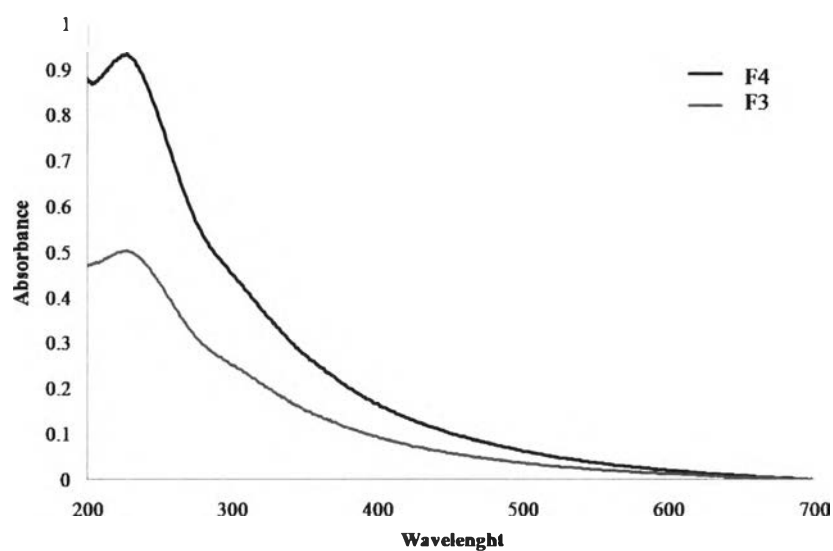


Figure 4. 3 UV absorption spectra of F3 (gray line) and F4 (black line) at final concentration of 8 ppm



#### 4.2.6 Selected area electron diffraction analysis (SAED)

To observe crystallographic orientation of graphite, graphene nanopellets (GNPs), F3 and F4, were analyzed by selected area electron diffraction analysis (SAED). SAED pattern from the multilayer region of graphite and GNPs are shown in Figure 4.4a - 4.4c. SAED pattern of graphite showed clear diffraction spots due to crystalline order (Figure 4.4a). SAED pattern of GNPs showed simple hexagonal pattern of sharp spots (Figure 4.4b and 4.4c). SAED pattern of F3 also showed simple hexagonal pattern of sharp spots (Figure 4.4d- 4.4e). SAED patterns of F4 showed diffused diffraction rings (Figure 4.4f) the diffraction dots (Figure 4.4g) and hexagonal pattern of sharp spots (Figure 4.4h), indicating disordered carbon structure of F4.

In summary, the hexagonal pattern was obtained in SAED patterns of graphite, GNPs and F3, not F4. It indicated that graphite, GNPs and F3 have crystalline structure<sup>56 184</sup>. SAED pattern of F4 which is many diffraction patterns indicates that F4 is amorphous or disordered structure. The SEAD result could be confirmed with TEM and HR-TEM images which showed the aggregation of many small spherical shapes. The result implies that the CCNs comprise of many small spherical shapes and small sheets aggregated together. So it indicates that F4 is aggregation of many ordered structure.





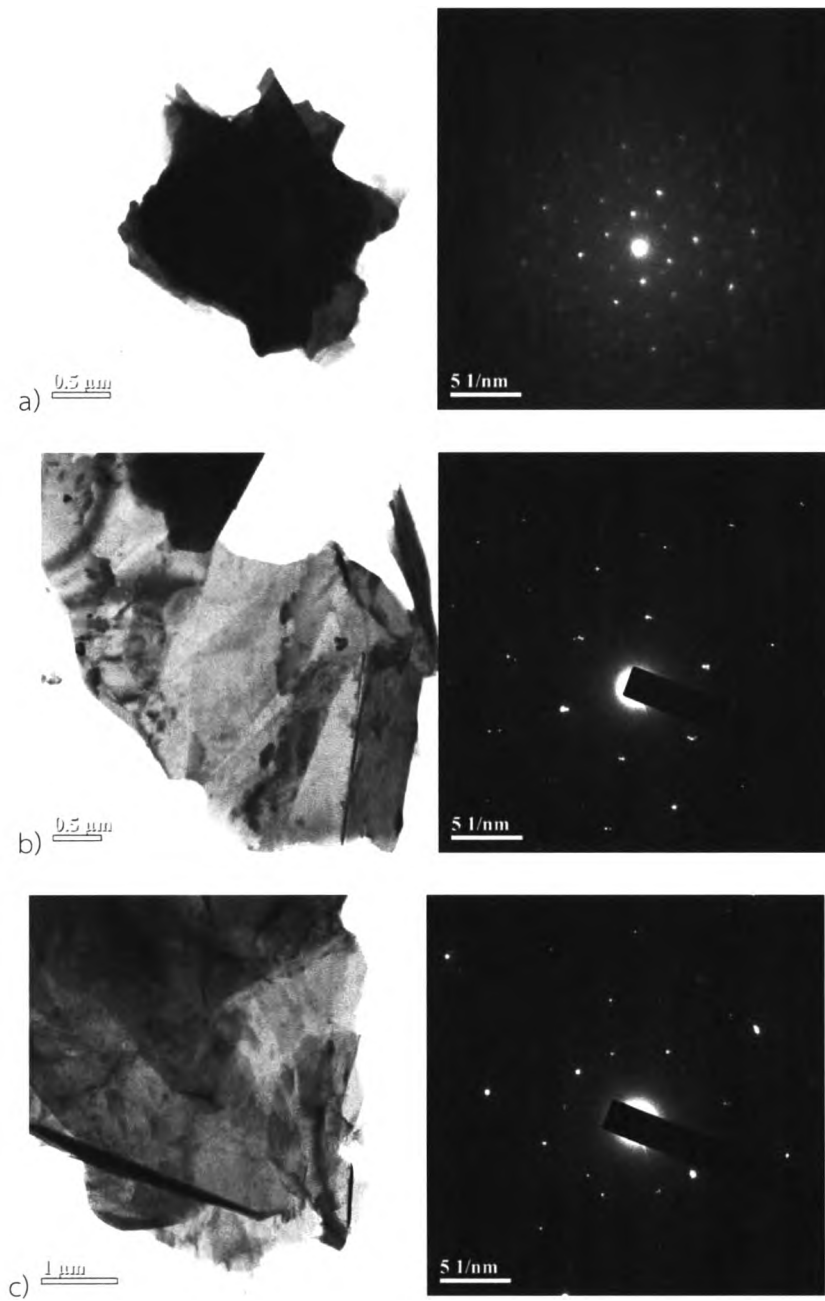


Figure 4. 4 TEM image (left) and SAED pattern (right) of graphite (a), graphene nanoplatelet (GNP) (b, c), F3 (d, e) and F4 (f-h)



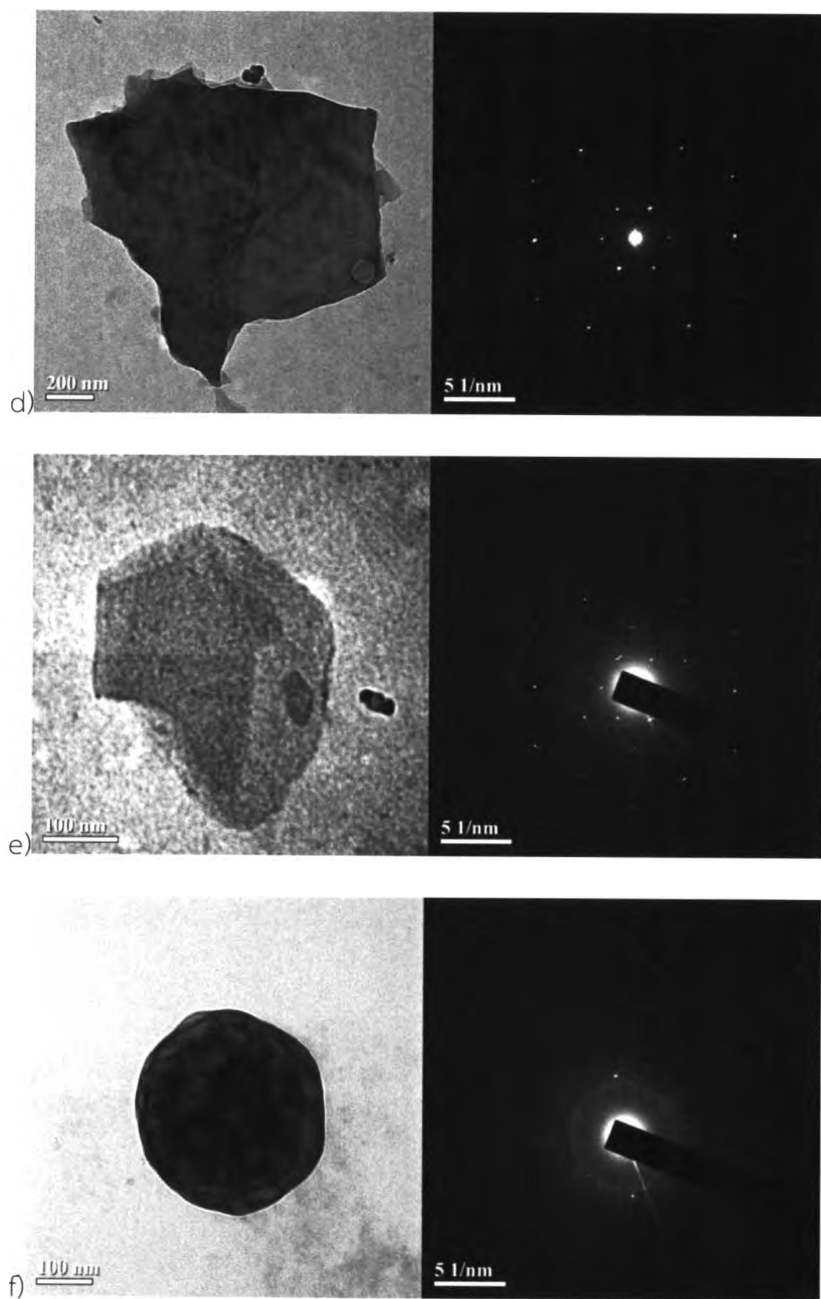


Figure 4. 4 TEM image (left) and SAED pattern (right) of graphite (a), graphene nanoplatelet (GNP) (b, c), F3 (d, e) and F4 (f-h) (continued)



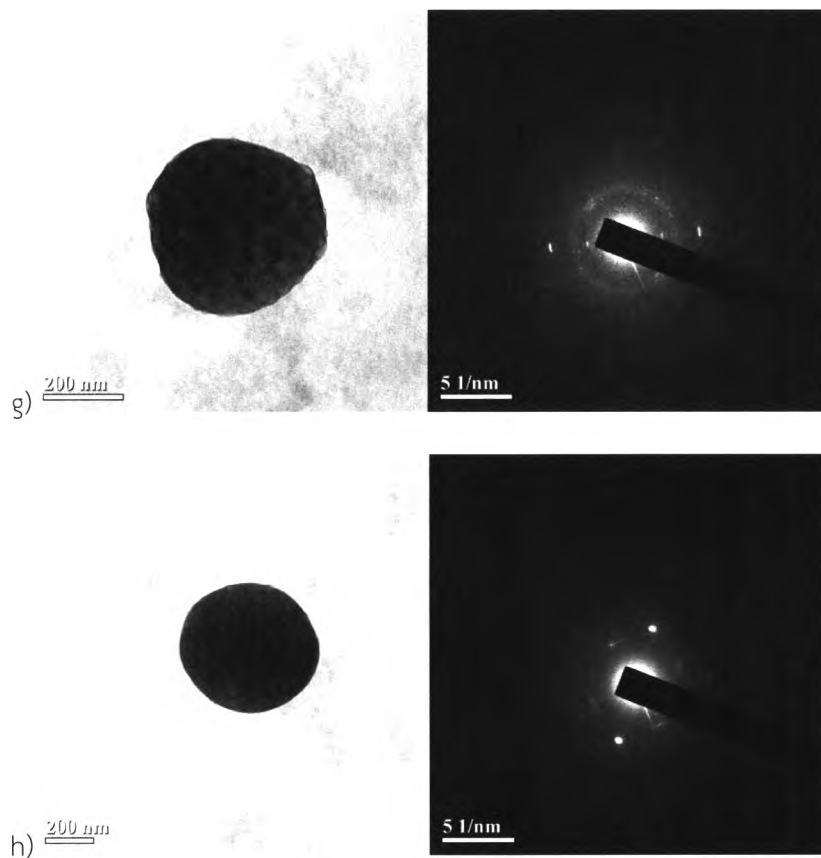


Figure 4. 4 TEM image (left) and SAED pattern (right) of graphite (a), graphene nanoplatelet (GNP) (b, c), F3 (d, e) and F4 (f-h) (continued)



#### 4.2.7 Attenuated total reflectance-fourier transform infrared spectroscopy (ATR-FTIR)

The functional group characterization of F4 was carried out by ATR-FTIR analysis. F4 suspension was freeze dried and then subjected to ATR-FTIR analysis. The ATR-FTIR spectrum of F4 showed a broad OH stretching at  $3,344\text{ cm}^{-1}$ , obvious C=C stretching at  $1,600\text{-}1800\text{ cm}^{-1}$ , O-H bending at  $1362\text{ cm}^{-1}$  and C-O stretching at  $1205\text{ cm}^{-1}$  (Figure 4.5). The result indicates that F4 is an oxidized product from the chemical exfoliation/oxidation of graphite.

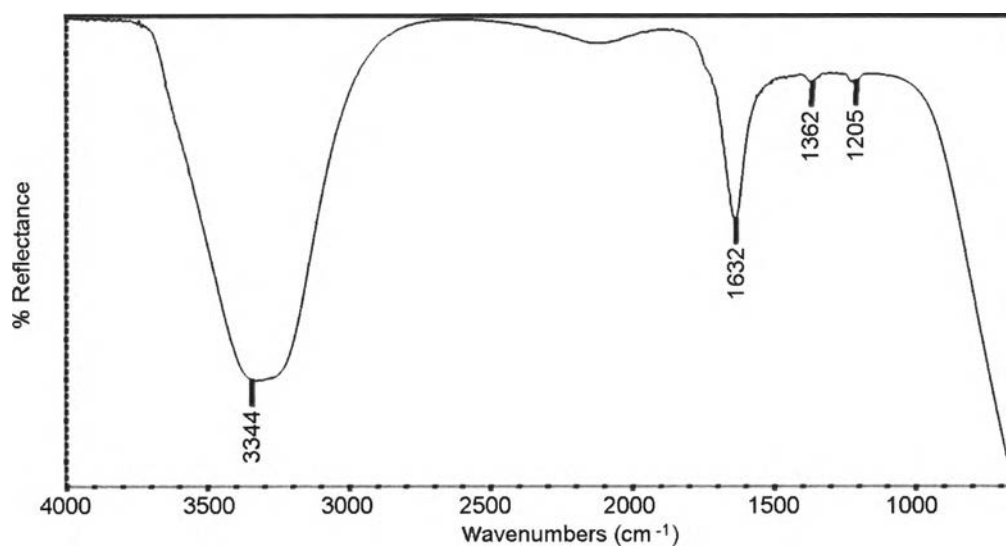


Figure 4. 5 FTIR spectrum of F4

เลขที่..... ๑๗. ๒๕๕๖  
 เลขทะเบียน..... ๗๒๐๑  
 วันเดือนปี..... ๑๖ ส.พ. ๒๕๖๐

#### 4.2.8 Raman spectroscopy

The structural characterization of graphite and F4 was also carried out by Raman spectroscopy. The vibration spectra of graphite and F4 are shown in Figure 4.6. The Raman spectrum of graphite showed peak at  $1312\text{ cm}^{-1}$  and  $1578\text{ cm}^{-1}$  referring to G band and D band, respectively. G band implies the disorder-induced vibrational peak of the  $\text{sp}^2$  carbon lattice. D band implies the stretching vibrations peak from the  $\text{sp}^2$ -hybridized carbon atoms. The Raman spectrum of F4 showed broader G and D bands with their slight blue shift at  $1329\text{ cm}^{-1}$  and  $1594\text{ cm}^{-1}$ , respectively. The Raman spectrum of F4 also showed an obvious shoulder at  $1750\text{--}1800\text{ cm}^{-1}$ , implying the structural deformation of the  $\text{sp}^2$ -hybrid carbon plane due to graphite amorphization<sup>184 185</sup>. The shoulder at  $1750\text{--}1800\text{ cm}^{-1}$  which correspond to the C=O functionality contains was absent from the Raman spectrum of graphite. This confirms that F4 contains carbonyl and hydroxyl groups in their carbon network structure.

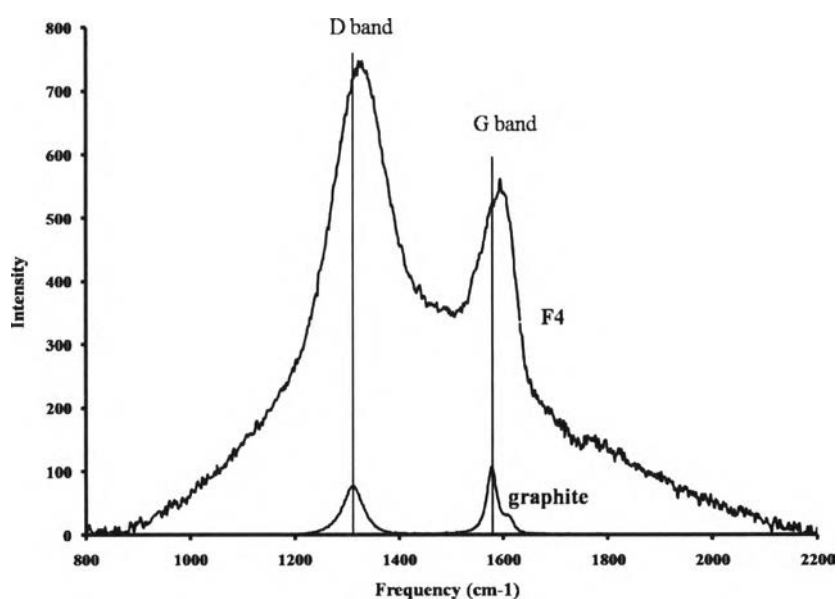


Figure 4. 6 Raman spectra of graphite and F4

#### 4.2.9 X-ray photoelectron spectroscopy (XPS)

X-ray photoelectron spectroscopy (XPS) is a surface-sensitive quantitative spectroscopic technique that measures the elemental composition. A typical XPS spectrum is plot of the number of electrons detected versus the binding energy (BE) of the electrons detected. Each functional group/element produces a characteristic set of XPS peaks at characteristic binding energy values. XPS analysis can determine the composition at the surface of the materials with binding energy values.

To investigate functional group at surface of carbon-based nanomaterials, XPS analysis was used. All samples, graphite, F3 and F4, were freeze dried and then subjected to XPS. XPS analysis of graphene oxide revealed the C-C, C=C, C-O (from C-O-C and C-OH), C=O and COOH functional groups which are C1s and O1s spectrums<sup>54 59</sup>. The BE of the C-C, C=C, C-O (from C-O-C and C-OH), C=O, and COOH functional groups from C1s spectrum are 283.6, 284.3, 286.3, 288.1 and 289.4 eV, respectively. The BE of the C-O (from C-O-C and C-OH), C=O, and COOH functional groups from O1s spectrum are 533.0, 531.7 and 530.5 eV, respectively. The summary of XPS results is shown in Table 4.6. The C1s spectrum of graphite showed BE at 284.0, 284.4, 286.0 and 290.0 eV referring to C-C, C=C, C=O and COOH functional groups, respectively. The O1s spectrum of graphite showed BE at 529.8 and 531.7 referring to C=O and COOH functional groups, respectively. The C1s spectrum of F3 showed BE at 284.0, 284.6, 286.7, 288.4 and 289.0 eV, referring to C-C, C=C, C-O, C=O and COOH functional groups, respectively. The O1s spectrum of F3 showed BE at 533.2, 532.0 and 530.6, corresponding to C-O, C=O and COOH functional groups, respectively. The C1s spectrum of F4 showed BE at 283.6, 284.3, 286.3, 288.1 and 289.4 eV refer to C-C, C=C, C-O, C=O and COOH functional groups, respectively. The O1s spectrum of F3 showed BE at 533.2, 532.0 and 530.6 refer to C-O, C=O and COOH functional groups, respectively. The XPS results indicated that F3 and F4 have carbonyl and hydroxyl functional groups at surface.



Table 4. 6 XPS analysis of graphite, F3 and F4 (see also appendix A)

Samples		Binding Energy (BE) (eV)	Functionality
Graphite	C1S	284.0, 284.4, 286.0, 290.0	C-C, C=C, C=O and COOH
	O1S	529.8, 531.7	C=O and COOH
Fraction 3	C1S	284.0, 284.6, 286.7, 288.4, 289.0	C-C, C=C, C-O, C=O and COOH
	O1S	530.6, 532.0, 533.2	C-O, C=O and COOH
Fraction 4	C1S	283.6, 284.3, 286.3, 288.1, 289.4	C-C, C=C, C-O, C=O and COOH
	O1S	530.5, 531.7, 533.0	C-O, C=O and COOH



#### 4.2.10 Elemental analysis (EA)

Quantitative analysis of the elemental composition of the carbon-based nanomaterials was identified by combustion elemental analysis. The C/O molar ratios of all samples are shown in Table 4.7. The C/O molar ratio of graphite, GNPs, F3 and F4 were 7.4, 12.7, 1.29 and 1.55, respectively. The two starting materials, graphite and GNPs, possesses higher C/O than F3 and F4. These indicated that F3 and F4 were heavily oxidized of the whole structure. Moreover, the C/O molar ratios of graphite, F3 and F4 calculated from XPS were 0.800, 0.428 and 0.295, respectively. XPS results corresponded to surface C/O composition of the material. The comparison between the C/O molar ratio of XPS and EA, indicated that the particle were more oxidized and/or hydrated at the surface. Furthermore, F3 and F4 were more oxidized than starting material, graphite. However, it should be noted that both the F3 and F4 were prepared in an aqueous environment and dried under vacuum, so it is very likely that some water molecules would be trapped in the materials, giving the low C/O ratios.

Table 4. 7 The C/O atomic ratios of graphite, GNPs, F3 and F4

Samples	C/O molar ratio	
	From combustion	From XPS
Graphite	7.43	0.800
GNP	12.7	Nd.
F3	1.29	0.428
F4	1.55	0.295

Nd. = not determined

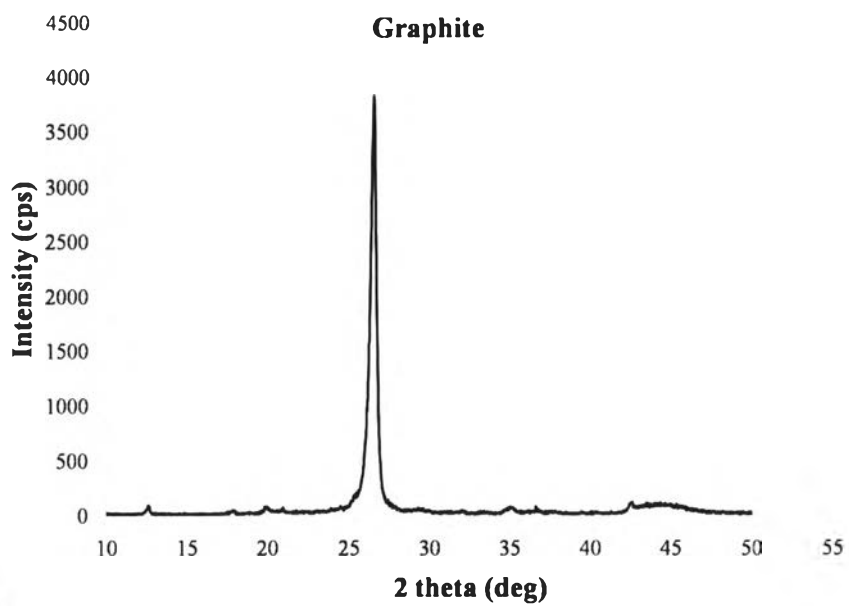




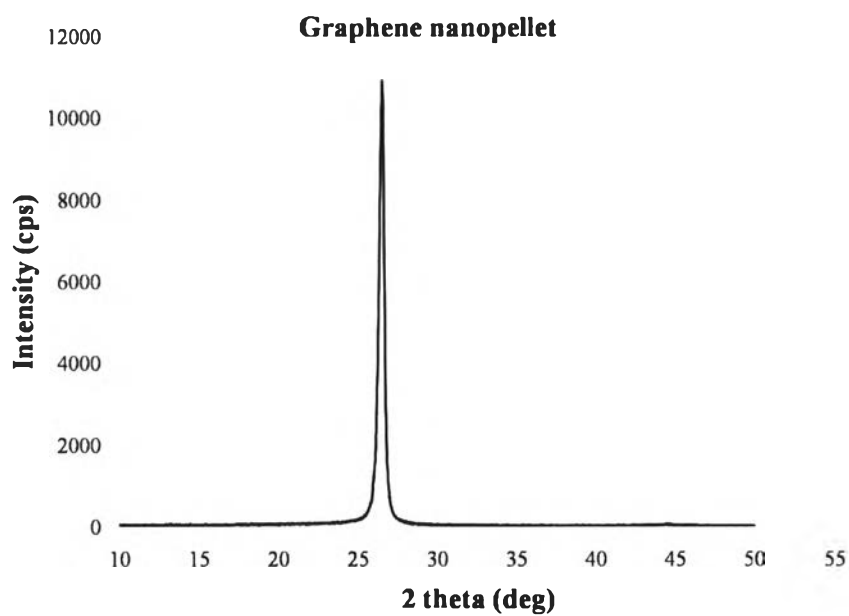
#### 4.2.11 X-ray diffraction analysis (XRD)

The crystallinity of graphite, graphene nanopellets (GNPs), F3 and F4, was determined by X-ray diffraction analysis. The XRD pattern of graphite and GNPs showed sharp peak around 26 degree (Figure 4.7a and 4.7b). The XRD pattern of F3 showed two small broad peaks at 10 and 26 degree (Figure 4.7c). The XRD pattern of the F4 showed a broad peak around 10 degree (Figure 4.7d). XRD results indicated that graphite and GNPs possess high crystalline structure which F3 and F4 were less crystallinity. This indicated that the oxidation of graphite and GNPs reduced crystallinity.





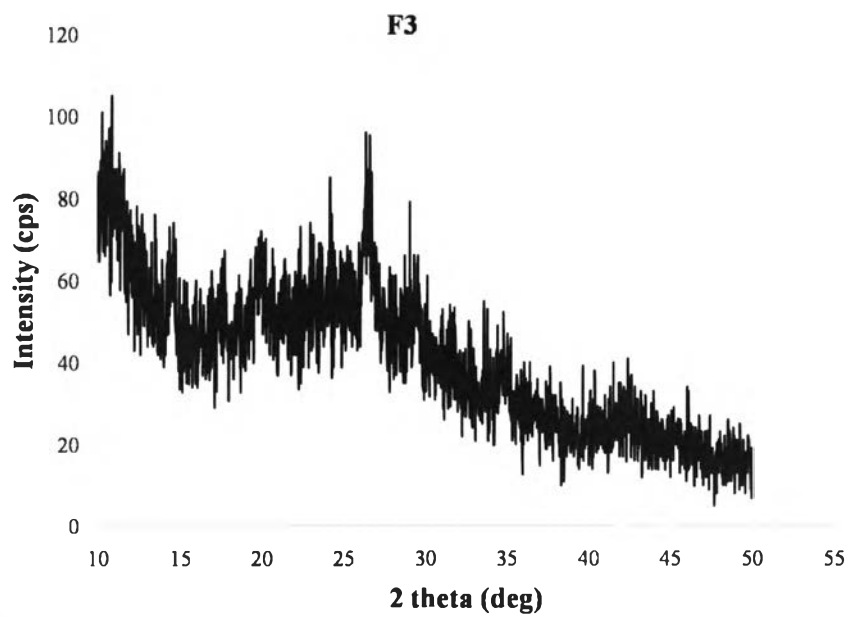
a)



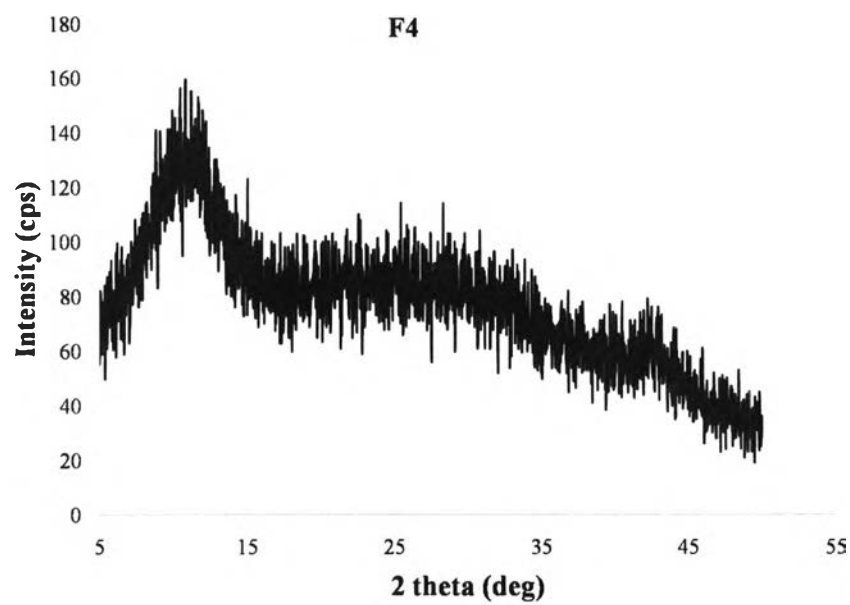
b)

Figure 4. 7 XRD patterns of graphite (a), GNPs (b), F3 (c) and F4 (d)





c)



d)

Figure 4.7 XRD patterns of graphite (a), GNPs (b), F3 (c) and F4 (d) (continued)



#### 4.2.12 Thermo-gravitational analysis (TGA)

The thermal properties of graphite, F3 and F4, were determined by thermo-gravimetric analysis. All the analyses have been conducted under the nitrogen atmosphere at 40 °C - 800 °C with a slow ramp rate of 5 °C/ min. The TGA curves of all samples are shown in Figure 4.8. The TGA curve of F3 and F4 showed a minor weight loss at 100 °C (~14%) which is referred to absorbed water. Another significant weight loss peak of F3 and F4 were at 130 - 280 °C (~28%). The weight loss was previously ascribed to the decomposition of oxidized carbon functional groups in form of CO, CO<sub>2</sub> and steam<sup>24</sup>. The weight loss at 400 - 800 °C is attributed to the sublimation and burning. The weight loss of graphite is small and steady whereas the weight loss of F3 and F4 are gradually decreased. The weight loss of F3 and F4 are in similar trend, indicating similar chemical structure of the two materials.



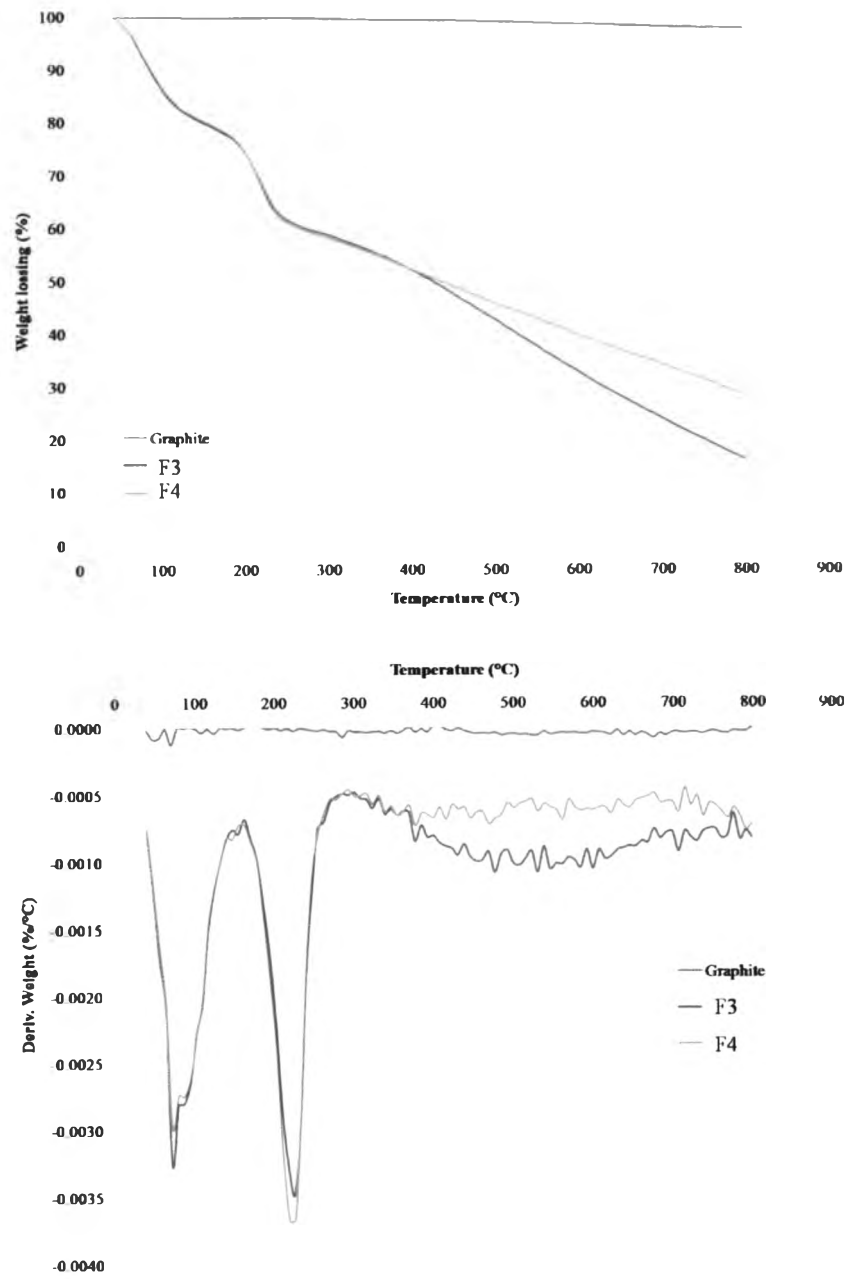


Figure 4. 8 TGA curve of graphite, F3 and F4



137614976

Summary of the characterizations are shown in Table 4.8. The SEM and TEM images reveal that graphene sheets were found in F1, F2 and F3 whereas the spherical particles were found in F4 and F5. HR-TEM of F3 show 6-8 layers stacking graphene sheet while F4 show aggregation of many small spherical structure. The ATR-FTIR, XPS and Raman spectroscopy spectrums indicated the F3 and F4 comprised of alkenyl, carbonyl and hydroxyl functional groups including; C=C, C-O, C=O, COOH and OH. The SAED and XRD results indicated that graphite and GNPs has high crystallinity structure, whereas F3 and F4 have lower crystallinity structure. The XPS and EA results indicated that F3 and F4 have higher oxygen content compared to graphite or GNPs. Furthermore, oxygen was on the surface rather than inside of the particles. The UV-Vis absorption spectra of F3 and F4 were similar with a maximum absorption at 227 nm and an extended absorption up to 600 nm implying presence of an extended  $\pi$ - $\pi$  conjugation network. The TGA curves of F3 and F4 showed a minor weight loss at 100 °C and 130–280°C due to absorbed water and decomposition of oxidized carbon functional groups whereas the weight loss of graphite is steady.

In conclusion, F3 is a several layer of stacking 100-300 nm carbon sheet with crystallinity structure, extended  $\pi$ - $\pi$  conjugation network and highly oxidized surface. Thus, this fraction is graphene oxide sheets (GOShs). F4 is 100-200 nm spherical structure comprised of many small spherical particles. The particles have deformed  $sp^2$ -hybrid carbon plane, extended  $\pi$ - $\pi$  conjugation network and highly oxidized surface. It indicated that F4 is cluster of carbon oxide nanospheres (CCNs). CCNs possesses good solubility with modifiable surface functional group and acceptable size for cellular endocytosis ( $>200$  nm)<sup>186</sup>. For these reasons, CCNs were selected as a novel nano-carrier for drug delivery system.



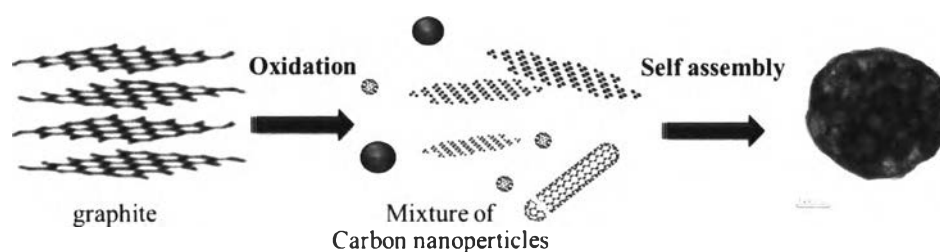


Figure 4. 9 Preparation of cluster of carbon oxide nanospheres (CCNs)

Table 4. 8 Morphology characteristics of carbon-based nanomaterials

Samples /Characterization	Fraction 1 (F1)	Fraction 2 (F2)	Fraction 3 (F3)	Fraction 4 (F4)	Fraction 5 (F5)
SEM	ND		ND		ND
TEM		ND			
HR-TEM	ND	ND			ND
Size from SEM	ND	ND	ND	110.8 ± 0.09	ND
Size from DLS	ND	ND	271.1 ± 7.22	132.1 ± 4.74	ND
ζ potential	ND	ND	-50.21 ± 0.73	-47.56 ± 1.18	ND
UV-vis spectroscopy	ND	ND	$\lambda_{\max}=227$ nm	$\lambda_{\max}=227$ nm	ND



Table 4. 8. Morphology characteristics of carbon-based nanomaterials (continued)

Samples /Characterization	Fraction 1 (F1)	Fraction 2 (F2)	Fraction 3 (F3)	Fraction 4 (F4)	Fraction 5 (F5)
SAED	ND	ND	crystalline	amorphous	ND
XRD	ND	ND	Low crystalline	amorphous	ND
FTIR	ND	ND		C=C, C=O and OH functional groups	ND
XPS	ND	ND	C-C, C=C, C-O, C=O and COOH functional	C-C, C=C, C-O, C=O and COOH functional	ND
the C/O molar ratio from XPS	ND	ND	0.428	0.295	ND
the C/O molar ratio from EA	ND	ND	1.29	1.55	ND

ND= not determine





### 4.3. Synthesis of TAMRA-CCN nanoparticles (CCNsT) and Curcumin-loaded TAMRA-CCN nanoparticles (CCNsT-C)

In order to follow the intracellular localization of drug deliver nano-partical inside target cells, nanoparticles needed to be labeled with fluorescent dye. Here, hydroxyl fuctional group on surface of CCNs can be modified with fluorescent dye as marker for fluorescence imaging. CCNs was covalently labeled with fluorescence dye, the fluorophore 5,6-carboxytetramethylrhodamine (TAMRA), to obtain the TAMRA-labeled cluster of carbon oxide nanoparticles (CCNsT) (Figure 4.10). TAMRA labeling of CCNsT was confirmed by UV- Vis spectrometry, SEM, DLS, and CLSFM.

There were two actives agent used as model drug in further experiments; curcumin and PNA. First, curcumin (1,7-bis(4-hydroxy-3-methoxyphenyl)-1,6-heptadiene-3,5-dione) is a potential bioactives that has been widely used in pharmaceutical field with many bioactivities including anti-tumor activity. Moreover, curcumin can be tracked rather conveniently because of its autofluorescent. However, curcumin contains an extensive  $\pi$ - $\pi$  conjugation with two aromatic moieties, therefore, hinder its water solubility. Curcumin-loaded CCNs (CCNs-C) and curcumin-loaded CCNsT (CCNsT-C) were prepared exploiting the ability to be absorbed on CCNs surface via  $\pi$ - $\pi$  stacking. CCNs-C and CCNsT-C were further characterized by UV-Vis spectrometry, SEM, DLS, and CLSFM.



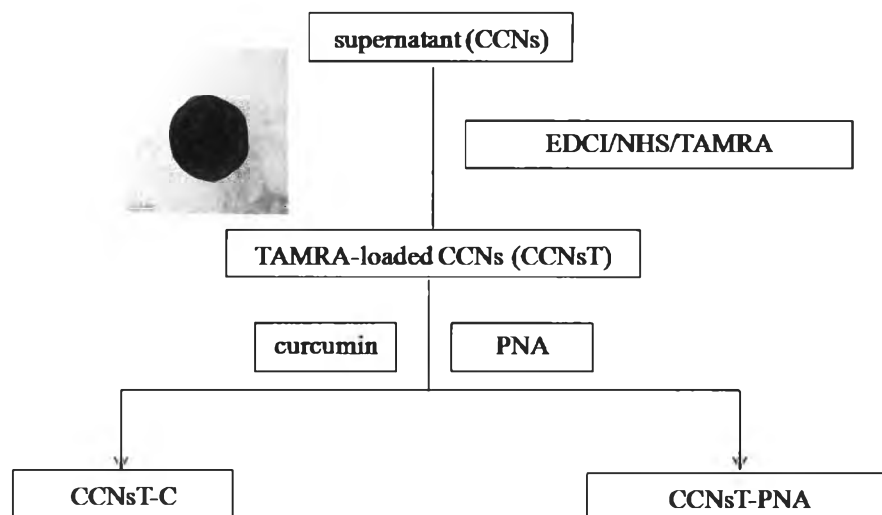


Figure 4. 10 Synthesis of TAMRA-labeled CCNs (CCNsT), TAMRA-labeled curcumin loaded CCNs (CCNsT-C) and TAMRA-labeled PNA loaded CCNs (CCNsT-PNA).



### 4.3.1 UV-Vis spectroscopy

To investigate the absorbance of TAMRA and curcumin, UV-Vis spectroscopy was used. The UV-Vis absorption spectra of CCNsT, CCNs-C and CCNsT-C suspension are shown in Figure 4.11. The absorption peaks at 430 nm and 565 nm (Figure 4.11; C and T) correspond to absorption of curcumin and TAMRA, respectively. These results confirmed that TAMRA can be labeled on to CCNs to obtain CCNsT via EDCI/NHS coupling reaction. Additionally, curcumin can be adsorbed on the CCNs and CCNsT surface via hydrophobic interaction.

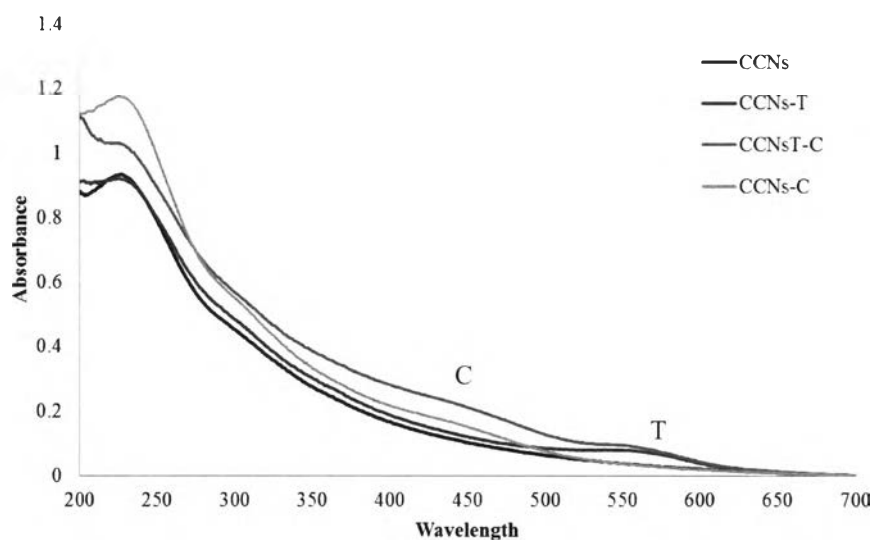


Figure 4. 11 UV absorption spectra of CCNs, TAMRA-labeled CCNs (CCNsT), TAMRA-labeled curcumin loaded CCNs (CCNsT-C) and curcumin loaded CCNs (CCNs-C)



137614976

### 4.3.2 Confocal laser scanning fluorescence microscopy (CLSM)

CCNsT and CCNsT-C were evaluated for their fluorescence under confocal laser scanning fluorescence microscopy. Figure 4.12a and 4.12b showed CLSM images of CCNsT in red spots (1000x magnification). Figure 4.12c show CLSM images of CCNsT-C were showed in yellow spot (1000x magnification with 4x digital zoom). Then CLSM image of CCNsT-C was unmixed using free curcumin and free TAMRA spectrum data base. The resulting images denoting labeled TAMRA and adsorbed curcumin were shown in Figure 4.12d left and right, respectively. These indicated that TAMRA and curcumin were stably deposited on CCNs surface and can be detectable using CLSM. Beside, CCNsT-C size was slightly larger than CCNsT under CLSM.



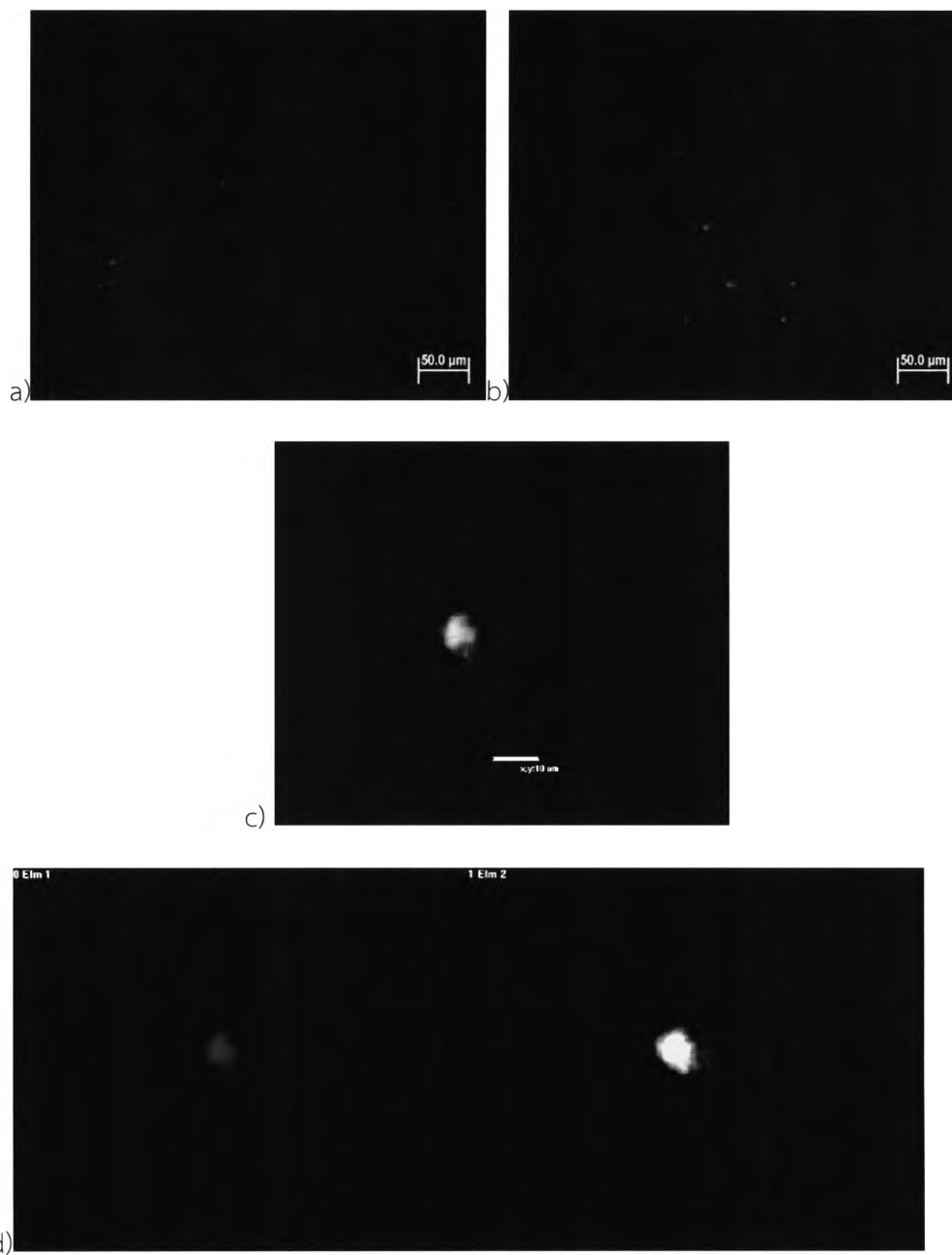


Figure 4. 12 CLSM image of CCNsT (a, b), CCNsT-C (c) and CCNsT-C unmixed (d)



### 4.3.3 Encapsulation efficiency (%EE) and active loading (% curcumin loading)

To calculate encapsulation efficiency and curcumin loading, UV-Vis spectroscopy was used. The curcumin was extracted from CCNs-C by absolute ethanol. The UV-Vis absorption spectrum of CCNs-C is shown in Figure 4.11. A calibration curve of curcumin in ethanol was constructed by measuring the absorbance of curcumin standard solution at 430 nm. The encapsulation efficiency and loading of curcumin was calculated by equation (1) and (2) (shown in Chapter III). The encapsulation efficiency was  $55.9 \pm 5.4\%$  (w/w of curcumin to initial curcumin) and curcumin loading was  $21.8 \pm 1.7\%$  (w/w of curcumin to curcumin-loaded CCNs).

### 4.3.4 Scanning electron microscopy (SEM) and dynamic light scattering (DLS)

Morphology of CCNsT and CCNsT-C were characterized by scanning electron microscope. SEM photographs of CCNsT and CCNsT-C (Table 4.9) showed aggregation of numeral small spherical structure similar to CCNs (Table 4.2). Size of CCNsT and CCNsT-C were determined by two methods, average dry particle size measurement from SEM and hydrated particle size calculated from DLS. The average diameter of CCNsT and CCNsT-C from SEM were  $127.8 \pm 25.8$  nm and  $209.3 \pm 101.4$  nm, respectively, on the other hand, the average hydrated diameter from DLS were  $261.1 \pm 4.53$  nm and  $425.25 \pm 21.29$  nm, respectively (Table 4.10). Comparing the three particles; CCNs, CCNsT and CCNsT-C, the dry particle size was gradually increased when labeled with TAMRA and loaded with curcumin. Hydrated particle of CCNsT and CCNsT-C were significantly larger compared to the corresponding dry particles. These may be caused by hydration sphere.

The surface charge of CCNs, CCNsT and CCNsT-C were  $-47.56 \pm 1.18$  mV,  $-36.56 \pm 1.92$  mV and  $-38.34 \pm 0.96$  mV, respectively. The zeta potential of CCNsT and CCNsT-C were similar and below  $-30$  mV but less changed than that of CCNs, indicating that both particle were stable in water solution<sup>183</sup> with more neutral (less negatively charged) surface compared to the highly oxidized surface of CCNs.



Table 4. 9 SEM photographs of CCNsT and CCNsT-C

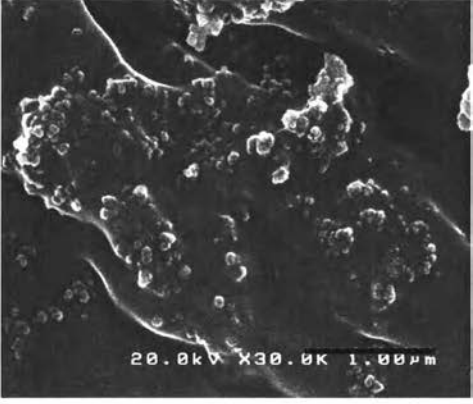
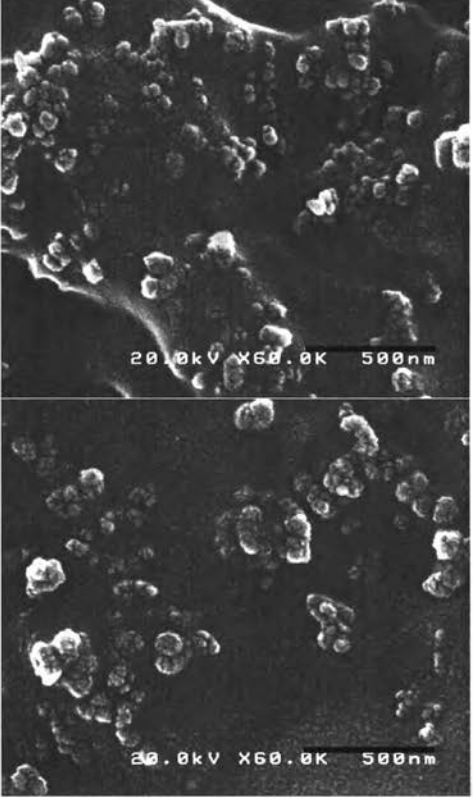
Samples	Magnification	Scale bar ( $\mu\text{m}$ )	SEM photographs
CCNsT	30,000x	1	
	60,000x	0.5	



Table 4. 9 SEM photographs of CCNsT and CCNsT-C (continued)

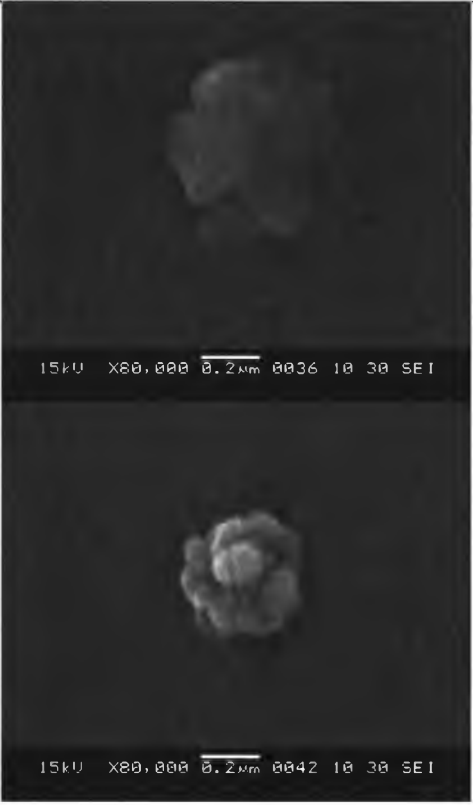

Samples	Magnification	Scale bar ( $\mu\text{m}$ )	SEM photographs
CCNsT	80,000x	0.2	
CCNsT-C	30,000x	1	





Table 4. 9 SEM photographs of CCNsT and CCNsT-C (continued)

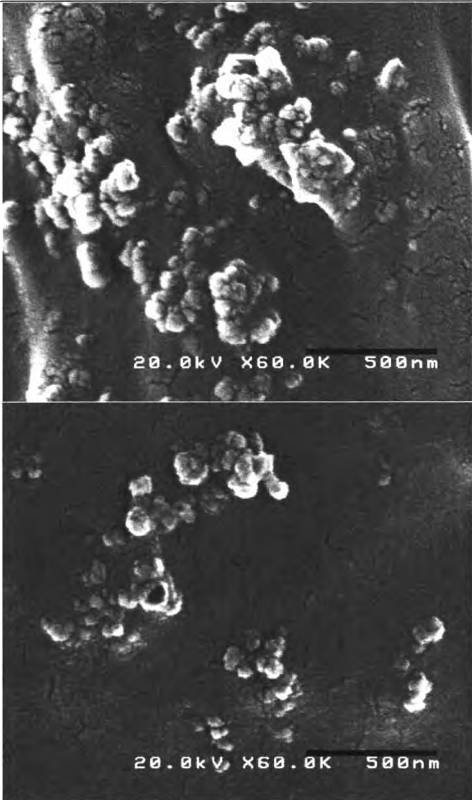
Samples	Magnification	Scale bar ( $\mu\text{m}$ )	SEM photographs
CCNsT-C	60,000x	0.5	

Table 4. 10 Physicochemical characteristics of CCNsT and CCNsT-C

Sample	Particle size distribution from SEM	Particle size distribution from DLS	PDI	$\zeta$ potential
CCNs	$110.8 \pm 0.09$	$132.1 \pm 4.74$	0.387	$-47.56 \pm 1.18$
CCNsT	$127.8 \pm 25.8$	$261.6 \pm 4.53$	0.430	$-36.56 \pm 1.92$
CCNsT-C	$209.3 \pm 101.4$	$425.25 \pm 21.29$	0.384	$-38.34 \pm 0.96$



#### 4.3.5 Assessment of cell viability for CCNs

To evaluate cytotoxicity of CCNs against human cells, the 3-(4,5-dimethylthiazol-2-yl)-2,5-diphenyltetrazolium bromide (MTT) mitochondrial activity assay was used. The human embryonic kidney 293 cells (HEK293T) and human epidermoid cervical carcinoma cells (CaSki) were used as a model system. The HEK293T cells and CaSki cells were pre-seeded into 96 well plates for 24 h and then were exposed to 0.01-10.0  $\mu\text{g/mL}$  CCNs for 48 h. At the CCNs concentrations of 1.0  $\mu\text{g/mL}$ , the cell viability was 102% and 90% for the HEK293T and CaSki cells, respectively (Figure 4.13). At higher concentration of CCNs of 10.0  $\mu\text{g/mL}$ , the cell viability decreased to 86% and 74%, respectively. The relatively low *in vitro* cytotoxicity of the CCNs indicated the biocompatibility of CCNs. The results indicated that CCNs is non-cytotoxic at concentrations of  $\leq 10.0 \mu\text{g/mL}$ .



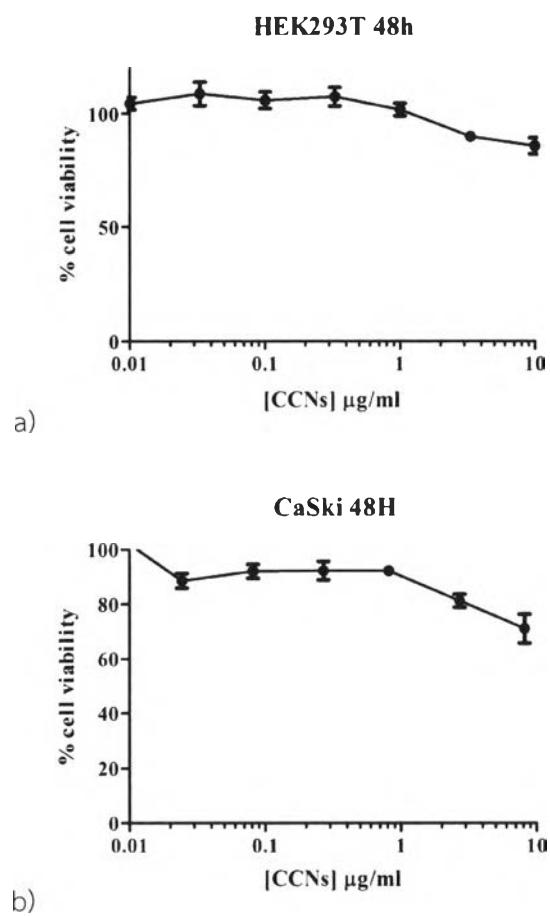


Figure 4. 13 Cytotoxicity of various concentrations of CCNs in HEK293T (a) and CaSki (b) cells after 48 h incubation as determined by MTT assay



#### 4.3.6 Cellular uptake of CCNsT-C

To track the cellular uptake and localization of CCNsT and curcumin *in vitro*, CLSFM was used. The HEK293T cells were placed on cover slip for 24 h and then were exposed to either free curcumin or CCNsT-C. After incubation with samples for 2 h, the cells were then thoroughly washed and stained with acridine orange (green). After that the sample was subjected to CLSFM analysis. The obtained fluorescent images from various areas were deconvoluted to obtain single fluorescent signal of curcumin, CCNsT and acridine orange. All the unmixing was carried out using Nikon-EZ-C1 gold v3.80 software. It was possible because the three emission spectra (curcumin, CCNs and acridine orange) were significantly different. The CLSFM images of free curcumin and CCNsT-C are shown in Figure 4.14. Autofluorescence of the curcumin is shown in yellow. The CCNsT is shown in red and acridine orange is shown in green. In this study, acridine orange stain corresponds to cytoplasm. The CLSFM images revealed both curcumin and TAMRA inside the cells at different localizations (Figure 4.14b). The curcumin fluorescence (yellow) was observed in the nucleus (Figure 4.14b2) whilst CCNsT (red) was found only in the cytoplasm (Figure 4.14b3). In the control experiment in which free curcumin at the same concentration was incubated with the cells (Figure 4.14a). The curcumin fluorescence was also observed only in the nucleus (Figure 4.14a2). The comparison between free curcumin and CCNsT-C, showed that without the CCNsT carriers, the uptake of curcumin into the cells was dramatically reduced. Therefore, it indicated that CCNs could be taken up by the cells and also used as drug carrier. Moreover, this implies that curcumin dissociated from the CCNsT carriers once inside the cells and then entered the nucleus.



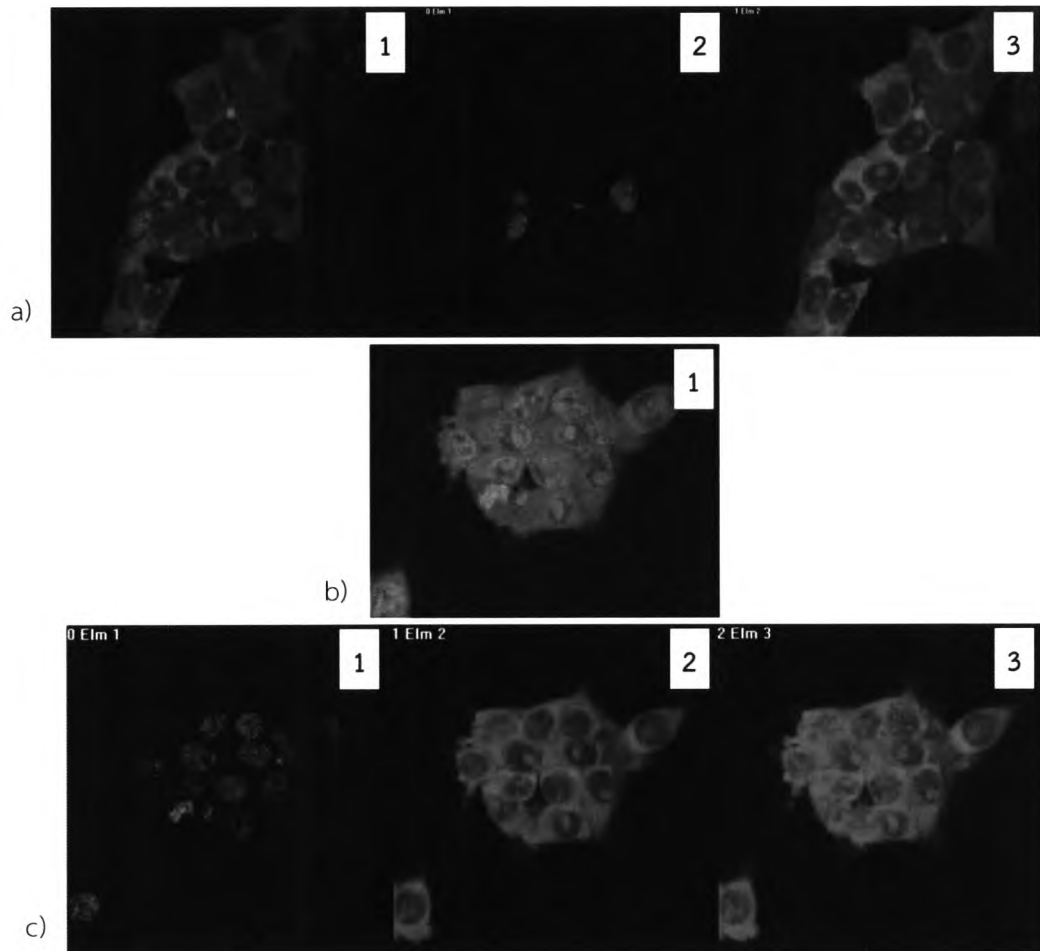


Figure 4. 14 CLSM images of free curcumin (a) and CCNsT-C (b)



#### 4.3.7 Anticancer activity of CCNs-C

To investigate anticancer activity, curcumin was used as a model drug since it was reported for high anticancer activity<sup>99 100 101 102</sup>. The anticancer activity of curcumin-loaded CCNs was evaluated *in vitro* with the human epidermoid cervical carcinoma (CaSki) cell lines. The 24 h pre-incubated CaSki cells were seed into a 96 well plates. Then the cells were exposed to samples; free curcumin (FC) in DME media (DMEM) and DMSO, CCNs and CCNs-C, in DMEM and incubated for 24 h. The final concentration of CCNs was 8.16 µg/mL and the final concentration of curcumin was 1.84 µg/mL. The anticancer activity graph is shown in Figure 4.15. The CCNs-C gave the lowest cell viability of around 54% whereas free curcumin in DMEM and DMSO gave cell viability of 91% and 76%, respectively. The lower activity of free curcumin is due to no intracellular transporter. The cell viability of CCNs was 76%. It indicated that CCNs can additively improve anti-tumor activity of curcumin probably through their own anti-tumor activity and their ability to effectively delivery curcumin into cells.

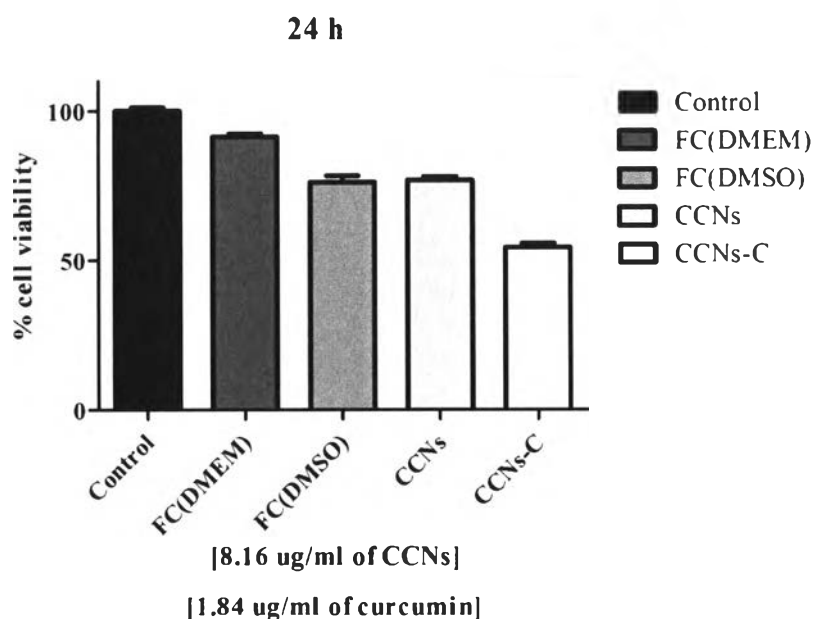


Figure 4. 15 Anticancer test of curcumin-loaded CCNs (CCNs-C), free curcumin (FC), and CCNs, on CaSki cells at 24 h incubation

These results indicated that CCNs can adsorb curcumin on its surface and release the materials once inside the cells. The localization of CCNs in cytoplasm implied its potential to be used as novel drug delivery system.

#### 4.4. PNA-loaded CCNs or CCNsT nanoparticles (CCNs-PNA or CCNsT-PNA)

PNA is an artificially synthesized polymer with N-(2-aminoethyl) glycine unit combined with peptide. It is resistance to degradation by nucleases and proteases<sup>134</sup><sup>187</sup>. Moreover, PNA shows greater specificity in binding to complementary sequence of DNA and mRNA<sup>137</sup><sup>138</sup>. At present, there is few report of successful delivered PNA to nucleus<sup>149</sup><sup>150</sup>. Many research discussed the recent progress and future goals in developing therapeutic PNAs against targeted nucleic acid sequences.

While curcumin plays role as cell permeable active<sup>111</sup>, PNA is cell impermeable active<sup>139</sup>. Thus, it is essential that the carrier for PNA needed to be able to carried PNA through cell membrane, release PNA inside the cell and not cause cytotoxicity. In this study, (1S, 2S)-2-aminocyclopentanecarboxylic PNA (acpcPNA) was used. The PNA sequences were designed specifically complemented to the nuclear factor kappa B (NF- $\kappa$ B) binding site in the promoter of *il-6* gene. The full construct of NF- $\kappa$ B specific sequences-labeled fluorescence dye was Flu-O-GGGATTTTCCCA-LysNH<sub>2</sub> (NF- $\kappa$ B<sub>flu</sub> PNA) used for intercellular trafficking test. The full construct of NF- $\kappa$ B specific sequences was Bz-GGGATTTTCCCA-LysNH<sub>2</sub> (NF- $\kappa$ B PNA) used for cytotoxicity test and IL-6 expression test. The full construct of random sequences-labeled fluorescence dye was Flu-O-TGTCAACTGACT-LysNH<sub>2</sub> (PNA<sub>flu</sub>) as negative control for intercellular trafficking test. The full construct of random sequences was Bz-TGTCAACTGACT-LysNH<sub>2</sub> (PNA) as negative control for cytotoxicity test and IL-6 expression test.

To prepare the samples, CCNs was incubated with PNA at 4°C for 24 h. The PNA<sub>flu</sub>-loaded CCNsT (CCNsT-PNA<sub>flu</sub>) and NF- $\kappa$ B<sub>flu</sub> PNA-loaded CCNsT (CCNsT- NF- $\kappa$ B<sub>flu</sub> PNA) were used for intercellular trafficking test. The PNA-loaded CCNs (CCNsT-PNA) and NF- $\kappa$ B-loaded CCNs (CCNs- NF- $\kappa$ B PNA) were used for cell viability and *il-6* gene expression test.



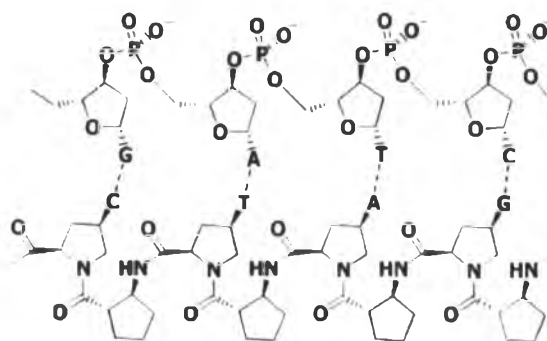


Figure 4. 16 Structure of DNA (blue) and (1S, 2S)-2-aminocyclopentanecarboxylic PNA (acpcPNA) (red)<sup>137</sup>

#### 4.4.1 Confocal laser scanning fluorescence microscopy (CLSM)

To confirm PNA was absorbed on CCNs surface, CLSM was used. NF- $\kappa$ B<sub>flu</sub> was used as model for PNA-labeled fluorescence dye. To prepare NF- $\kappa$ B<sub>flu</sub> PNA-loaded CCNs (CCNs- NF- $\kappa$ B<sub>flu</sub> PNA), CCNs was incubated with NF- $\kappa$ B<sub>flu</sub> PNA at 4°C for 24 h under light-proof condition. The final concentrations of NF- $\kappa$ B<sub>flu</sub> PNA and CCNs were 10  $\mu$ M and 1 mg/ml, respectively. The free NF- $\kappa$ B<sub>flu</sub> PNA solution was used as negative control. After incubation, the CCNs- NF- $\kappa$ B<sub>flu</sub> PNA was placed on to glass slide and then subjected to CLSM. The CLSM images of free NF- $\kappa$ B<sub>flu</sub> PNA and CCNs-NF- $\kappa$ B<sub>flu</sub> PNA are shown in Figure 4.17. The fluorescence signal of NF- $\kappa$ B<sub>flu</sub> PNA exhibited in green. The CLSM image of free NF- $\kappa$ B<sub>flu</sub> PNA solution showed slightly green (Figure 4.17a). The CLSM image of CCNs-NF- $\kappa$ B<sub>flu</sub> PNA showed green spot (Figure 4.17b). It indicated that NF- $\kappa$ B<sub>flu</sub> was absorbed on CCNs surface.





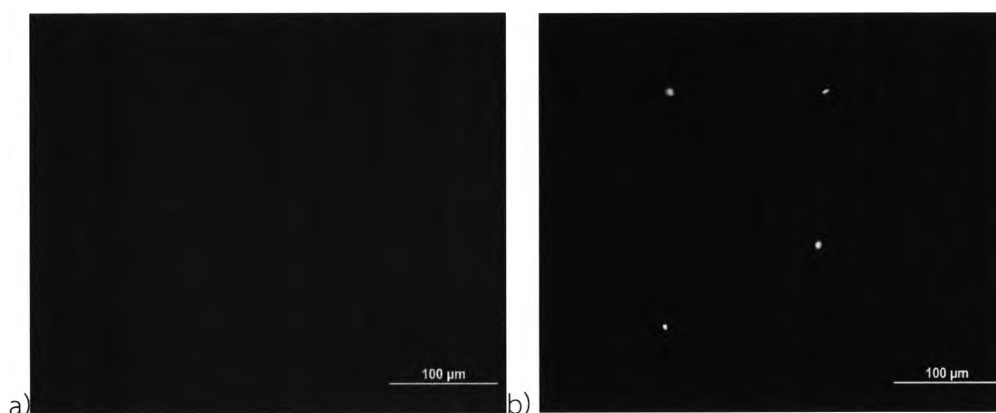


Figure 4. 17 CLSM of free NF- $\kappa$ B<sub>flu</sub> (a) and CCNs- NF- $\kappa$ B<sub>flu</sub> (b)

#### 4.4.2 PNA loading

According to the CLSM result of CCNs-NF- $\kappa$ B<sub>flu</sub> PNA (Figure 4.17), the PNA molecules are embedded physically in to the matrix or absorbed onto the surface. The CLSM image showed clear green spot with no background interfering. It indicated that free NF- $\kappa$ B<sub>flu</sub> PNA was not remained. To calculate PNA loading, the amount weights of NF- $\kappa$ B<sub>flu</sub> PNA and CCNs were calculated using equation (2). Ten microliter of NF- $\kappa$ B<sub>flu</sub> PNA (100  $\mu$ M in PBS pH 7.4) was used. The weight of NF- $\kappa$ B<sub>flu</sub> PNA was 4.29  $\mu$ g. Hundred microliters of CCNs was used at the concentration of 1 mg/mL. The weight of CCNs was 100  $\mu$ g. Then PNA loading was 4.15% (w/w)

#### 4.4.3 Assessment of cell viability for NF- $\kappa$ B PNA

NF- $\kappa$ B PNA was designed specifically to complement with the nuclear factor kappa B (NF- $\kappa$ B) binding site of the promoter of *il-6* gene. Interleukin 6 (IL-6) is a cytokine that plays important role in acute inflammatory response. IL-6 can be induced in macrophage. Then Mouse leukaemic monocyte macrophage cell line (RAW 264.7 cells) was used for IL-6 expression test including cytotoxicity test.

To investigate the toxicity of samples, free NF- $\kappa$ B, CCNs and CCNs- NF- $\kappa$ B, the *in vitro* cell viability was determined by MTT assay. The 24 h pre-incubation, RAW 264.7 cells were seeded into a 96 well plates. Then cells were exposed to samples at various concentrations, in the range of 0.1-10  $\mu$ g/mL, for 24 h. After incubation, cell viability was measured. As shown in Figure 4.18, the CCNs at concentration of 0.1-10.0  $\mu$ g/mL showed more than 75% of the cell viability. The free NF- $\kappa$ B PNA and

CCNs-NF- $\kappa$ B PNA at concentration of 0.1-10.0  $\mu$ g/mL showed more than 80% of the cell viability. The result indicated that all samples were non-cytotoxicity at concentration of 0.1-10.0  $\mu$ g/mL. In addition, it is important to note that NF- $\kappa$ B PNA is not toxic to this cell type.

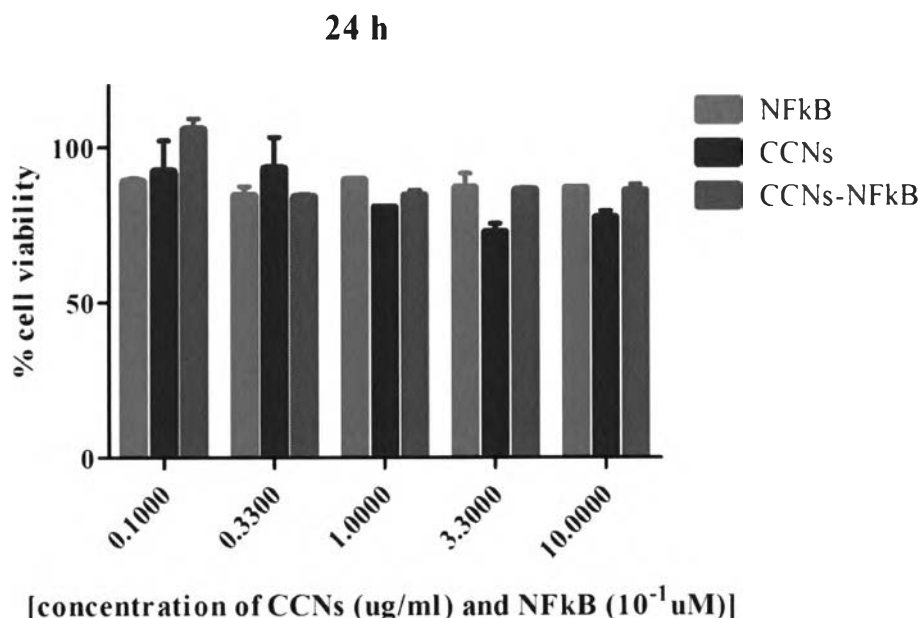


Figure 4. 18 In vitro toxicity test of RAW 264.7 cells exposed to various concentration of free NF- $\kappa$ B, CCNs and CCNs-NF- $\kappa$ B

#### 4.4.4 Cellular uptake of CCNsT-PNA<sub>flu</sub> and CCNsT-NF- $\kappa$ B<sub>flu</sub> PNA

To prove CCNs as nanocarriers for drug delivery system, the cellular uptake of CCNsT-PNA<sub>flu</sub> and CCNsT-NF- $\kappa$ B<sub>flu</sub> PNA was investigated. To study the uptake of CCNsT-PNA<sub>flu</sub> and CCNsT-NF- $\kappa$ B<sub>flu</sub> PNA by RAW 264.7 cells, CLSM was used. RAW 264.7 cells were placed on cover slip for 24 h and then were exposed to samples (free PNA<sub>flu</sub>, free NF- $\kappa$ B<sub>flu</sub> PNA, PNA<sub>flu</sub>-loaded CCNsT and NF- $\kappa$ B<sub>flu</sub> PNA-loaded CCNsT). RAW 264.7 cells were incubated with samples for 4 h. The final concentration of PNA<sub>flu</sub> and CCNs were 0.5  $\mu$ M and 5  $\mu$ g/mL, respectively. The cells were fixed. The nucleus stained (in blue) with DAPI dye. After that, CLSM was used to track the location of NF- $\kappa$ B<sub>flu</sub> PNA or PNA<sub>flu</sub> and the CCNsT inside the cells. The obtained fluorescent signals from various areas were then deconvoluted for fluorescent spectra of NF- $\kappa$ B<sub>flu</sub> PNA or PNA<sub>flu</sub>, Dapi and CCNsT. All the unmixing was carried out

using image algorithms and it was possible because the three spectra were significantly different. CLSM images of RAW 264.7 cells as control are shown in Figure 4.19a. In Figure 4.19b and 4.19c, CLSM images showed that the free PNA<sub>flu</sub> and free NF- $\kappa$ B<sub>flu</sub> PNA were slightly able to permeate cell membranes without carriers (arrows). Figure 19d and 19e clearly demonstrate that PNA<sub>flu</sub> and NF- $\kappa$ B<sub>flu</sub> PNA (green) did not co-localise any longer with the CCNsT (red) after being internalised by RAW 264.7 cells. In case of CCNsT-PNA<sub>flu</sub> (Figure 4.19d), the fluorescence signal of PNA<sub>flu</sub> (green) was found in the nucleus and cytoplasm. It indicated PNA<sub>flu</sub> was accumulated in the nuclei of cells, seen as round structures positioned in the centre of the cell. The fluorescence signal of CCNsT (red) was found in cytoplasm. The results indicate that the CCNsT are mainly observed outside the nuclei within the cytoplasm. Areas in the cell where PNA<sub>flu</sub> and CCNsT colocalise can be observed along the border between the cytoplasm and the nucleus, the so-called “nuclear envelope”, and on the cell membrane. In another case, CCNsT- NF- $\kappa$ B<sub>flu</sub> PNA (Figure 4.19e), the fluorescence signal of NF- $\kappa$ B<sub>flu</sub> PNA (green) was also found in the nucleus with unique dots formation. It indicated that NF- $\kappa$ B<sub>flu</sub> PNA was accumulated in the nuclei of cells. The fluorescence signal of CCNsT (red) was also found mainly in cytoplasm. This result demonstrates that CCNs can be used as nanocarriers for PNA delivery system. Moreover, in case of CCNsT-NF- $\kappa$ B<sub>flu</sub> PNA, NF- $\kappa$ B<sub>flu</sub> PNA was localized as dots formation distributes, punctate pattern, in the nucleus which is called “speckled nuclear localization”<sup>188 189 190</sup>. The result implies that NF- $\kappa$ B<sub>flu</sub> PNA which is specific NF- $\kappa$ B sequence could bind with DNA at NF- $\kappa$ B binding site. It should be noted that NF- $\kappa$ B<sub>flu</sub> may form PNA-DNA complexes which can be visualize as a punctate fluorescence signal.



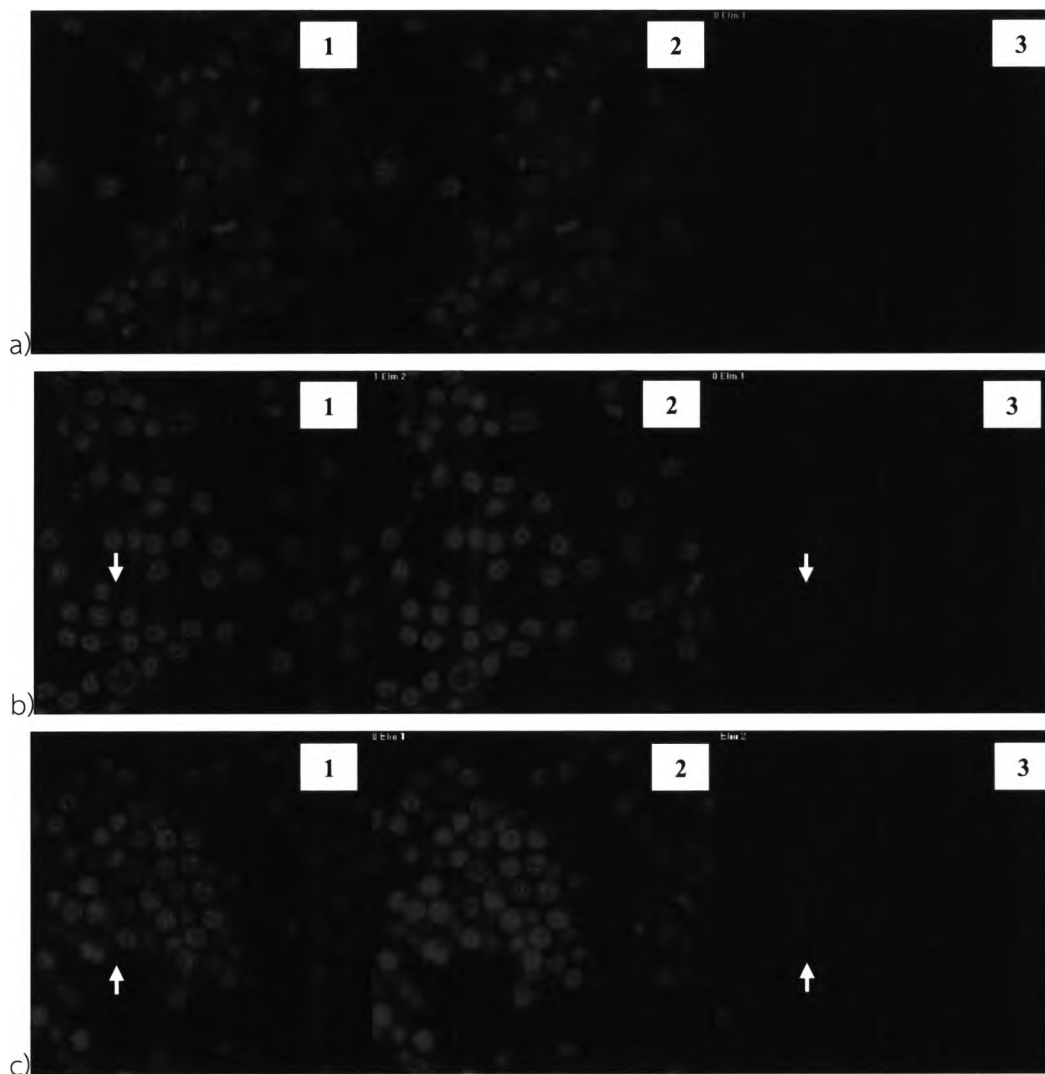


Figure 4. 19 Multiple color staining CLSM images of RAW 264.7 cells negative control (a,1-3) and after being incubated with free random PNA<sub>flu</sub> (b,1-3), free NF-κB<sub>flu</sub> (c,1-3), random PNA<sub>flu</sub>-loaded CCNsT (d,1-4) and NF-κB<sub>flu</sub>-loaded CCNsT (e,1-4) for 4 h at 37 °C under 5% (v/v) CO<sub>2</sub>. Images, as the (a1-e1) original or (a (2-4)-e (2-4)) unmixed fluorescence signals of PNA<sub>flu</sub> or NF-κB<sub>flu</sub>, CCNsT and Dapi, shows in green, red and blue, respectively



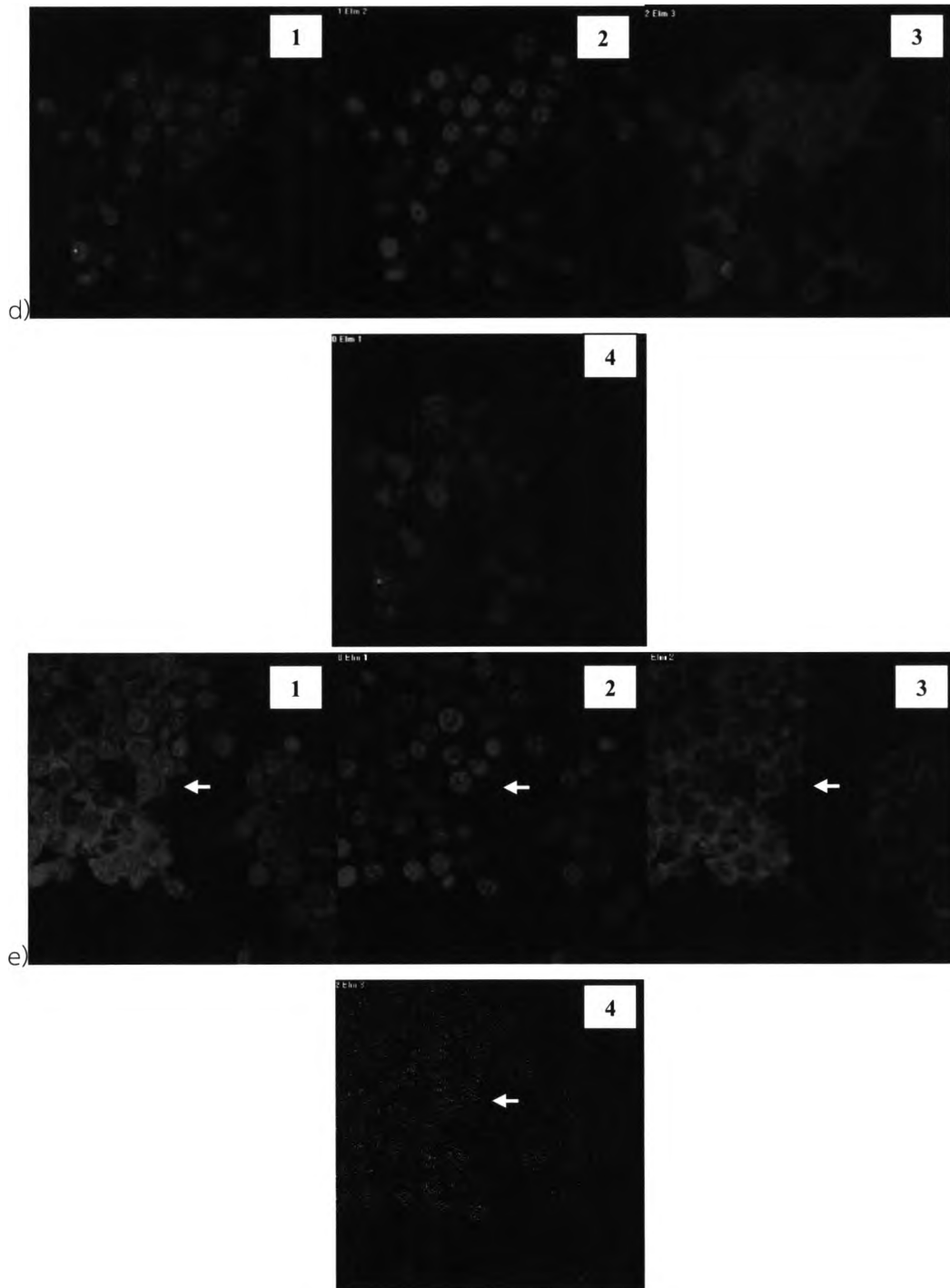


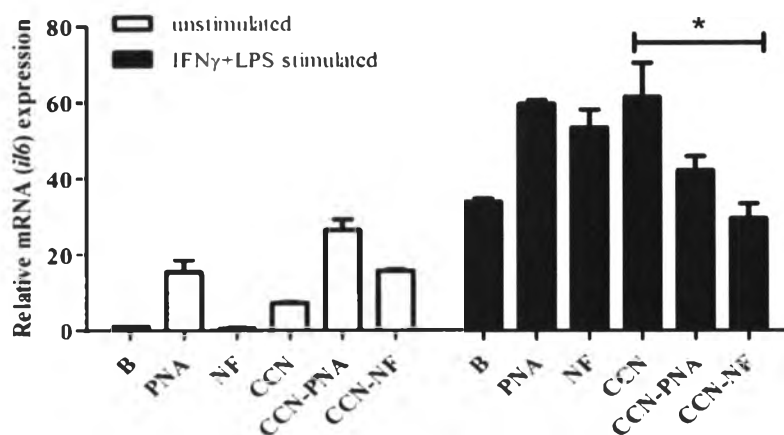
Figure 4.19 Multiple color staining CLSM images of RAW 264.7 cells negative control (a,1-3) and after being incubated with free random PNA<sub>flu</sub> (b,1-3), free NF-κB<sub>flu</sub> (c,1-3), random PNA<sub>flu</sub>-loaded CCN<sub>ST</sub> (d,1-4) and NF-κB<sub>flu</sub>-loaded CCN<sub>ST</sub> (e,1-4) for 4 h at 37 °C under 5% (v/v) CO<sub>2</sub>. Images, as the (a1-e1) original or (a

(2-4)-e (2-4)) unmixed fluorescence signals of PNA<sub>flu</sub> or NF- $\kappa$ B<sub>flu</sub>, CCNsT and Dapi, shows in green, red and blue, respectively (continued).

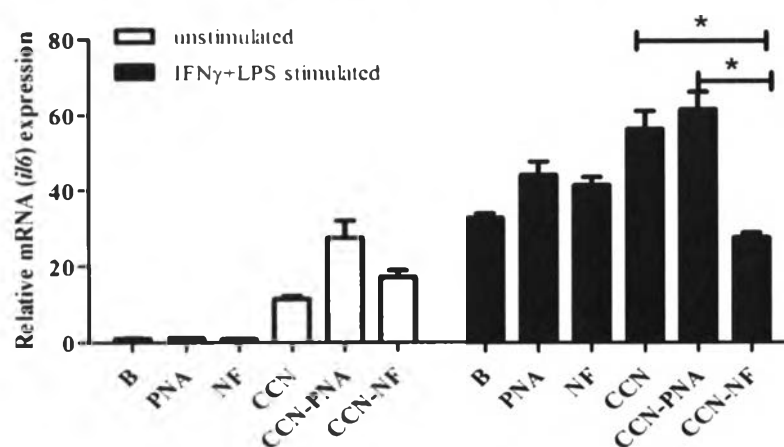
#### 4.4.5 The effect of *il-6* mRNA expression

To investigate *il-6* mRNA expression, IL-6 expression was induced through NF- $\kappa$ B pathway. The promoter region of the *il-6* gene revealed the presence of a binding site for the NF- $\kappa$ B transcription factor<sup>172 173</sup>. The action of NF- $\kappa$ B on the IL-6 promoter mediates is related to the regulation of IL-6 expression. The RAW 264.7 cells were incubated with samples for 2 or 4 h. The samples were the aqueous suspensions of free random PNA, free NF- $\kappa$ B PNA, CCNs, CCNs-PNA and CCNs-NF- $\kappa$ B PNA at final concentration of 5  $\mu$ g/mL of CCNs and 0.5  $\mu$ M of PNA or NF- $\kappa$ B PNA. Then the cells were inflammatory stimulated by LPS and IFN $\gamma$  for 6 h, after that total RNA was extracted. The level of *il-6* mRNA of all samples at 4 h of incubation is shown in Figure B1 (in Appendix B). The results were not repeatable. It might be caused by long incubation time due to the effect of CCNs on inflammation. So the incubation time was reduced to 2 h. Figure 4.20 (a-c) showed levels of *il-6* mRNA in LPS and IFN $\gamma$ -costimulated RAW 264.7 cells at 2 h. The result showed that the level of *il-6* mRNA of CCNs-NF- $\kappa$ B PNA was lower than stimulated positive controls; control, free random PNA and free NF- $\kappa$ B. It implied that CCNs-NF- $\kappa$ B PNA could suppress *il-6* mRNA expression. Nevertheless the level of *il-6* mRNA of LPS and IFN $\gamma$ -costimulated of CCNs-PNA, also showed lower *il-6* mRNA level expression than stimulated controls. So these results also were not repeatable. It might be caused by designed PNA sequence is not suitable or stable to bind to DNA.

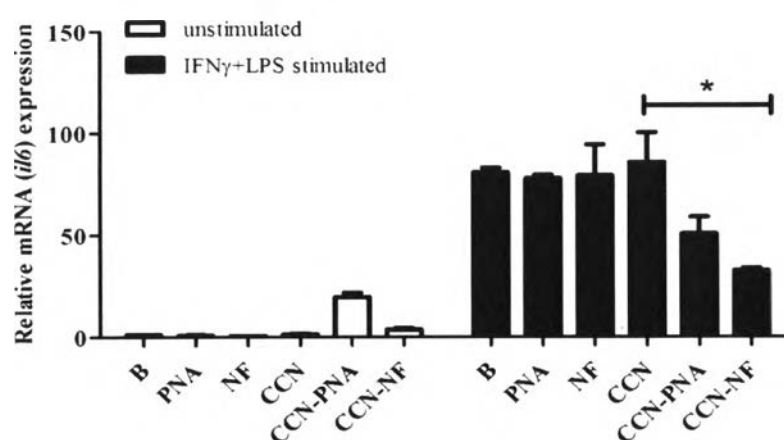




a)



b)



c)

\* indicated the statistically significant differences between conditions at  $p < 0.05$

Figure 4. 20 Effects of free random PNA, free NF- $\kappa$ B PNA, CCNs, CCNs-PNA and CCNs-NF- $\kappa$ B PNA on the levels of *il-6* mRNA in LPS plus IFN $\gamma$ -stimulated RAW 264.7 cells at 2 h (a-c) of incubations



137614976

#### 4.4.6 PNA-DNA binding

To analyze PNA-DNA binding, the gel electrophoresis was used. The gel electrophoresis is a method for separation and analysis of macromolecule, DNA, RNA and protein. It is use in molecular biology to separate a mixed population of DNA and RNA fragments by length. The separation of macromolecule bases on their size and charge.

In this study, DNA which is double stand was dissociated by heat at 95 °C for 10 min. After that the excess samples; free PNA, free NF- $\kappa$ B PNA and free NF- $\kappa$ B<sub>FLU</sub> PNA, were immediately added into DNA solution. The mixture solution was incubated for 2 h on ice bath. The mixture solution was then separated among PNA, DNA and PNA-DNA complexes, by gel electrophoresis. The result is shown in Figure 4.17. The result showed that all samples band were same position. If PNA can bind with DNA, it should be show different position, at higher Mw. Moreover, it can be confirmed by fluorecence exposed (Figure 4.17 lower). The fluorecence band of NF- $\kappa$ B<sub>FLU</sub>-DNA complex (Figure 4.17 lower) was not exhibited in the same position with EtBr stained (Figure 4.17 upper). The result indicated that PNA cannot bind with DNA. According to the personal commutation with Vilaivan, T.<sup>191</sup>, the concentration of PNA has effect to DNA binding. The concentrations of PNA, excess to 1 pmol, were analyzed. PNA can bind with DNA since same concentration of DNA to lower concentration of DNA. Moreover, the incubation time also has effect to PNA-DNA binding. 10 pmol of PNA was incubated with DNA various times, 1 min to 60 min. The result showed that the incubation time increase whereas the PNA-DNA complex decrease. As a consequence, it indicated that PNA can bind to DNA but it is detached when the time passed.





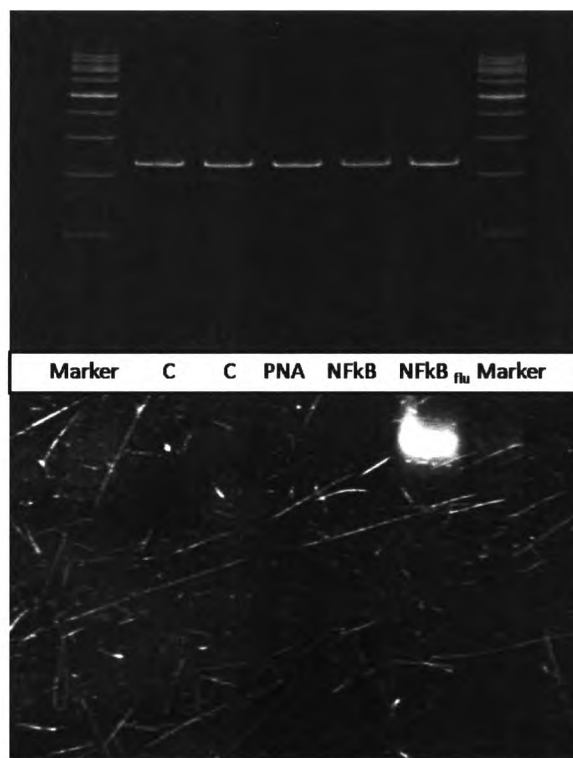


Figure 4. 21 Gel electrophoresis of PNA-DNA binding in 10% acrylamide gel: EtBr exposed (upper) and fluorescence exposed (lower)

